Implementation and testing of high voltage system for pulsed low-energy positron beam and conventional positron beam studies in InN

Antti Pelli

Laboratory of Physics
Helsinki University of Technology
Espoo, Finland

Dissertation for the degree of Doctor of Science in Technology to be presented with due permission of the Department of Engineering Physics and Mathematics for public examination and debate in Auditorium E at Helsinki University of Technology (Espoo, Finland) on the 2nd of February, 2007, at 13 o'clock.

Dissertations of Laboratory of Physics, Helsinki University of Technology
ISSN 1455-1802

Dissertation 145 (2007):
Antti Pelli: Implementation and testing of high voltage system for pulsed low-energy positron beam and conventional positron beam studies in InN
ISBN 978-951-22-8593-8(print)
ISBN 978-951-22-8594-5(electronic)

Otamedia OY
ESPOO 2007

Abstract

Positron annihilation spectroscopy is one of the few methods to study atomic scale lattice imperfections. The conventional positron lifetime spectroscopy is limited to bulk samples and a lifetime beam is required for measurements in epitaxially grown thin layers. This work describes the operation of the TKK pulsed positron lifetime beam with a grounded sample. Particularly, the unique high voltage realizations and challenges of HV design are discussed in detail. Thorough high voltage withstand tests are performed for every component in the HV system of the lifetime beam. Additionally, to protect electronics against breakdown induced transients, multi-stage transient suppressors are constructed and tested.

The timing properties of the lifetime beam are determined using electrons and positrons. A fast multichannel plate is utilized as a detector for the resolution measurements. Higher detector count rate and a brighter beam are achieved with electrons to accelerate the testing procedure. The time resolution of 160 ps observed for the lifetime beam is sufficient for positron lifetime measurements in semiconductors. The peak-to-background ratio is also sufficient, more than 5000.

A conventional continuous slow positron beam is used to study indium nitride grown by metal-organic chemical vapor deposition. The observed indium vacancy concentration of $\sim 10^{17}$ cm^{-3} is almost independent on the V/III molar ratio at 4800–24000. At lower ratios, below 4000, the In droplet formation is accompanied by the formation of vacancy clusters. The In vacancy formation depends on the growth temperature. The concentration increases from 9×10^{16} cm^{-3} to 7×10^{17} cm^{-3} when the growth temperature is increased from 550°C close to the decomposition temperature of 625°C.

Finally, 2 MeV $^4He^+$ irradiated InN grown by molecular beam epitaxy and gallium nitride grown by metal-organic chemical vapor deposition are studied. In GaN, the Ga vacancies act as important compensating centers in the irradiated material, introduced at a rate of 3600 cm^{-1}. The In vacancies are introduced in InN at significantly lower rate of 100 cm^{-1} making them negligible in the compensation of the irradiation-induced additional n-type conductivity. On the other hand, negative non-open volume defects are introduced at a rate higher than 2000 cm^{-1}. We propose that these defects are related to N interstitials and ultimately limit the free electron concentration at high irradiation fluences.

Tiivistelmä

Positroniannihilaatiospektroskopia on yksi harvoista menetelmistä, joilla voidaan tutkia atomiskaalan hilavirheitä. Perinteinen positronin elinajan mittausmenetelmä on rajoittunut paksujen näytteiden tutkimiseen ja siksi positronin elinajan mittaamiseen ohutkalvoissa tarvitaan elinaikasuihkua. Tämä työ kuvaa TKK:lla sijaitsevan pulssitetun positronisuihkun toimintaa. Kyseisen mittauslaitteen ainutlaatuinen korkeajännitetoteutus ja korkeajännitesuunnittelun haasteet käsitellään yksityiskohtaisesti. Jokainen laitteiston komponentti on suurjännitetestattu perusteellisesti. Lisäksi moniportainen suojaus on rakennettu ja testattu laitteiston elektroniikan suojaamiseksi syöksyjännitteitä vastaan.

Elinaikasuihkun ajoitusominaisuudet on määritetty sekä elektroneilla että positroneilla, käyttäen hiukkasilmaisimena nopeaa monikanava-analysaattoria. Elektroneja käyttämällä saavutetaan korkeampi ilmaisimen pulssitaajuus ja laadukkaampi hiukkassuihku kuin positroneilla ja näin laitteiston testaus nopeutuu. Määritetty laitteiston aikaresoluutio, 160 ps, on riittävä positronin elinaikamittauksiin puolijohteissa. Myös saavutettu piikki/tausta -suhde, suurempi kuin 5000, on riittävä.

Perinteistä jatkuvaa hitaiden positronien suihkua on käytetty tässä työssä MOCVD-menetelmällä kasvatetun indiumnitridin tutkimiseen. Havaittu indiumvakanssikonsentraatio, $\sim 10^{17}$ cm^{-3}, on lähes riippumaton V/III -moolisuhteesta välillä 4800–24000. Matalammilla V/III -suhteilla, alle 4000, kasvatettujen näytteiden pinnalla havaitun indiumpisaramuodostumisen todettiin liittyvän vakanssiklustereiden muodostumiseen. Indiumvakanssien muodostuminen riippuu myös kasvatuslämpötilasta. Vakanssikonsentraatio kasvaa 9×10^{16} cm^{-3}:sta 7×10^{17} cm^{-3}:een kun kasvatuslämpötilaa kasvatetaan 550°C:sta lähelle InN:n hajoamislämpötilaa, 625°C.

Lopuksi tässä työssä tutkittiin 2 MeV $^4He^+$ säteilytettyä MBE-kasvatettua indiumnitridiä ja MOCVD-kasvatettua galliumnitridiä. Säteilytetyssä galliumnitridissä galliumvakanssit toimivat tärkeinä kompensoivina keskuksina, joita syntyy nopeudella 3600 cm^{-1}. Indiumvakansseja syntyy indiumnitridissä huomattavasti vähemmän, 100 cm^{-1}, joten ne eivät kompensoi merkittävästi n-tyyppistä johtavuutta. Toisaalta, negatiivisia hilavirheitä muodostuu nopeudella 2000 cm^{-1}. Näiden voidaan olettaa olevan virheitä, jotka liittyvät typen välisijaan ja rajoittavat vapaiden elektronien tiheyden kasvamista suurilla säteilytysannoksilla.

Preface

This thesis has been prepared in the Positron Group of the Laboratory of Physics at the Helsinki University of Technology during the years 2002–2006. I wish to thank Prof. Pekka Hautojärvi for giving me the opportunity to work in this experimental group.

I am indebted to my supervisors Dr. Filip Tuomisto and late Prof. Kimmo Saarinen. I am grateful to my closest colleagues Floris Reurings and Antti Laakso for fruitful collaboration. I wish to thank the technical staff of the Laboratory of Physics, especially Klaus Rytsölä for providing me with useful knowledge concerning all technical challenges I faced. I thank all the members of the positron group for creating a pleasant working environment and maintaining lively discussions dealing with scientific and less scientific fields.

The financial support from the Jenny and Antti Wihuri foundation, Vilho, Yrjö and Kalle Väisälä foundation and Emil Aaltonen foundation is gratefully acknowledged.

I would like to express my gratitude to my parents, sister and especially Terhi for all the support, encouragement and Hope they have provided during the years.

Espoo, October 2006

Antti Pelli

Contents

List of publications

This thesis consists of an overview and the following publications:

I A. Laakso, A. Pelli, K. Rytsölä, K. Saarinen, and P. Hautojärvi. *Determination of the timing properties of a pulsed positron lifetime beam by the application of an electron gun and a fast microchannel plate,* Applied Surface Science **252**, 3148 (2006).

II A. Laakso, M. O. Hakala, A. Pelli, K. Rytsölä, K. Saarinen, and P. Hautojärvi. *Scattering effects in a positron lifetime beam line,* Material Science Forum **445-446**, 489 (2004).

III A. Pelli, A. Laakso, K. Rytsölä, R. Aavikko, M. Rummukainen, and K. Saarinen. *HV design of a pulsed lifetime beam with a grounded sample,* Materials Science Forum **445-446**, 504 (2004).

IV A. Pelli, A. Laakso, K. Rytsölä, and K. Saarinen. *The design of a main accelerator for a pulsed positron beam,* Applied Surface Science **252**, 3143 (2006).

V A. Pelli, K. Saarinen, F. Tuomisto, S. Ruffenach, and O. Briot. *Influence of V/III molar ratio on the formation of In vacancies in InN grown by metal-organic vapor-phase epitaxy,* Applied Physics Letters **89**, 011911 (2006).

VI A. Pelli, F. Tuomisto, K. M. Yu, and W. Walukiewicz. *Compensating point defects in He-irradiated n-type InN and GaN,* Helsinki University of Technology Publications in Engineering Physics, Report TKK-F-A846 (2006).

The author has had an active role in all the phases of the research reported in this thesis. The author has had an active role in the designing of the measurement system and in testing procedures described in Publ. I. He has participated in the measurements and improvement of the lifetime beam presented in Publ. II. He has had an active role in designing of the equipment and high voltage system described in Publ. III. He has carried out simulations, designing, assembly and testing of the high voltage structures introduced in Publ. IV. The author has performed the measurements and data-analysis and contributed to the interpretation of the results in Publs. V and VI. He has been the corresponding author of Publs. III–VI.

Chapter 1

Introduction

Semiconductors have unique electrical and optical properties. The ability to control the electrical conductivity of semiconductors through doping with impurities has revolutionized electronic devices during the last five decades. Also the photon interaction with charge carriers in semiconductor materials has been utilized in many optical applications which are becoming more and more important in different areas of everyday life. LEDs, solar cells and a variety of laser applications, e.g. CD/DVD player, are all based on semiconductor optoelectronics. The electronic and optical properties of semiconductors are greatly affected by lattice defects. Intensive research must be done on various semiconductor materials to improve their quality in order to further enhance the properties of semiconductor devices and to develop new ones.

Materials can be improved and growth processes understood only through studies of atomic scale lattice imperfections. The identification of these kind of defects is possible with only a few methods. Positron annihilation spectroscopy (PAS) is one of these. It is sensitive particularly to vacancy-type defects and can be applied for instance to semiconductor materials. Defect studies with positron annihilation spectroscopy consist of two main methods: Doppler broadening and lifetime spectroscopy. Both are easily applied to several hundreds of microns thick bulk samples, which are not available in all materials. Studies on thin material layers require more specific equipment, slow positron beams. Conventional continuous slow positron beams for Doppler measurements are in routine use, but positron lifetime beams are still uncommon. Nowadays, there exist only two fully operational beams; one in Munich, Germany [1] and one in Tsukuba, Japan [2].

This thesis consists of two parts: development and testing, in particular the high voltage (HV) design, of a positron lifetime beam and application of a conventional slow positron beam to studies of vacancy defects in indium nitride (InN). First

the methods of positron annihilation spectroscopy are shortly introduced. The concept of the TKK positron lifetime beam is described and its timing properties quantitatively determined. These tests and improvements of the pulsing system of the lifetime beam is the subject of Publs. I and II. The next chapter discusses in more detail the high voltage challenges and realization of the grounded-sample beam (Publs. III and IV). Publications V and VI form the second part of this thesis reporting the results from the InN studies. In Publ. V the effect of the V/III molar ratio and temperature in the metal-organic chemical vapor deposition (MOCVD) growth process on the crystal quality of InN are studied. A study on compensating point defects in irradiated n-type InN grown with molecular beam epitaxy (MBE) is reported in Publ. VI.

Chapter 2

Experimental methods in positron annihilation spectroscopy

Positron annihilation spectroscopy (PAS) is a common term for measurements of e.g. the lifetime and Doppler broadening of positron-electron annihilation radiation, which are useful in defect studies. The PAS techniques are based on the localization of positrons at lattice defects and the detection of the annihilation radiation of the positron-electron pair.

After entering the sample, positrons slow down within a few picoseconds (10^{-12} s) via various interactions with the lattice atoms. The positron diffuses as a thermalized particle within the sample. At room temperature the positron diffusion length is of the order of 100 nm. While diffusing, the positron probes the lattice and can get trapped at a vacancy where the potential is lower due to the missing positive ion core or at a Rydberg state around a negatively charged ion. If the positron is trapped at a vacancy, its lifetime is increased due to the decreased electron density. This is utilized in the positron lifetime measurements. While the positron lifetime reflects the size of open volume in the lattice, i.e. size of the vacancy, the Doppler broadening measurement gives information about the atoms surrounding the vacancy. By combining these two methods, PAS is a powerful technique to observe the structure and concentration of defects, its charge state as well as the surrounding impurity atoms. Vacancies are detected in the concentration range of 10^{15}–10^{19} cm^{-3}. The principles of the positron lifetime and Doppler broadening measurements are presented in Fig. 2.1.

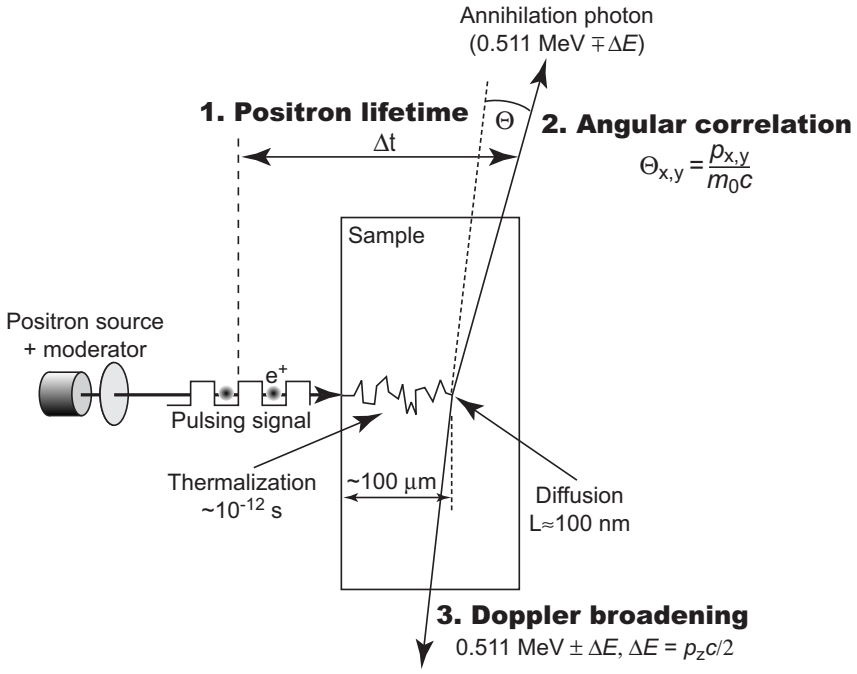

Figure 2.1: The positron annihilation spectroscopy techniques are lifetime, Doppler broadening and angular correlation measurements. In the conventional lifetime method, the use of the pulsing signal is replaced with the e^+ emission photon.

2.1 Conventional positron methods

2.1.1 Conventional lifetime spectroscopy

The conventional positron lifetime measurement is based on the detection of the gamma quantum emitted in the decay process of a β^+ radioactive isotope, e.g. ^{22}Na. The time difference between this emission photon and the annihilation photon is measured, and the positron lifetime(s) can be resolved from the time distribution containing $\sim 10^6$ lifetime events. The distribution can consist of several exponential lifetime components τ_i and the corresponding intensities I_i, i.e.

$$N(t) = \sum_i \frac{I_i}{\tau_i} e^{-t/\tau_i}. \tag{2.1}$$

The different positron lifetimes are associated with annihilations at different positron states. If no defects are observed, the spectrum is reduced to $N(t) =$

$\frac{1}{\tau_B}e^{-t/\tau_B}$, where τ_B is the positron lifetime in the bulk. Two typical lifetime spectra are shown in Fig. 2.2, measured in gallium nitride (GaN) on both growth polarities (Ga and N), where the average positron lifetimes were measured as 161 ps and 192 ps, respectively [3].

The average lifetime τ_{ave} of the positrons can be directly calculated as the center of mass of the lifetime spectrum. It is also the superposition of lifetimes of positrons annihilating in different states.

$$\tau_{\text{ave}} = \eta_B \tau_B + \sum_{i=1} \eta_{D,i} \tau_{D,i}. \tag{2.2}$$

The positron trapping fractions ($\eta_{D,i}$) for different vacancy types can also be estimated [4] and used in data analysis of Doppler broadening spectroscopy, especially in the 2D-Doppler measurements, where they can be used to decompose the Doppler spectrum. A decomposed spectrum enables more accurate identification of atoms surrounding the vacancies. The positron lifetimes can also be used in estimation of defect concentrations.

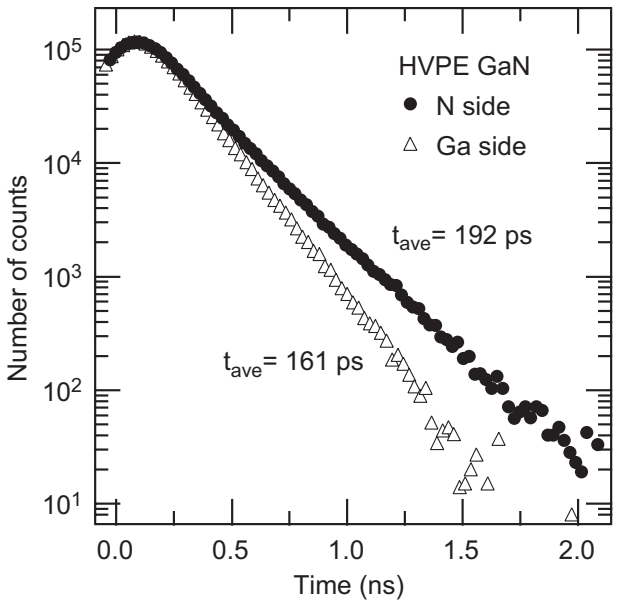

Figure 2.2: Positron lifetime spectra measured in GaN grown with both Ga and N polarities.

Measurement setup In the conventional lifetime measurement a ^{22}Na isotope source is sandwiched between two sample pieces. Due to the continuous energy

distribution of positrons extending up to energies of 540 keV, thick (>100 μm) samples must be used to ensure that the positrons annihilate within the sample. This restricts the studied materials to such where thick bulk samples can be grown. Two detectors, consisting usually of a plastic scintillator and a photomultiplier tube, are used: one to detect the 1.27 MeV emission photon and another one for the annihilation photon. The time difference between the observations is converted to voltage by a time-to-amplitude converter (TAC) and recorded by a multi-channel analyzer into a lifetime spectrum.

2.1.2 Doppler broadening spectroscopy

Due to the conservation of momentum in the annihilation process, annihilation radiation contains information on the electron momentum distribution at the annihilation site. This is used in the Doppler broadening measurement to study the electronic structure near the vacancy and identify e.g. the sublattice of a vacancy in compound semiconductors.

In the annihilation process the momentum of the annihilating positron-electron pair, $\mathbf{p}$, is transferred to the photon pair, whose energies are Doppler shifted from the initial 511 keV by amounts of $\pm\Delta E = p_z c/2$, where p_z is the projection of the momentum $\mathbf{p}$ in the propagation direction of the γ-rays. This shift is observed as the broadening of the measured annihilation line.

From the measured Doppler spectra a low-momentum parameter S (typically $|E - 511\ keV|$ <0.7 keV) and a high-momentum parameter W (2.6< $|E - 511\ keV|$ <7.5 keV) are calculated (see Fig. 2.3) to represent the shape of the Doppler broadened annihilation line. These parameters can be used to identify the defects e.g. by plotting the W parameter as a function of the S parameter in a (S,W) plot. In the case of only one vacancy type in the lattice, data points fall on a straight line. The slope of the line can be used in identification of the vacancy type [5]. The defect concentrations can also be estimated from the Doppler parameters using the standard positron trapping model [4].

Measurement setup Doppler broadening measurements are done routinely with both fast and slow positrons. In these measurements the energy of a annihilation photon is measured with a high-resolution energy-dispersive detector (1D-Doppler), or two collinear detectors may be used to measure both of the annihilation photons (2D-Doppler). Linear amplifiers, analog-to-digital converters and stabilizers are used to process the detector signals for a multi-channel analyzer which records the energies into a histogram.

In positron annihilation spectroscopy, measurements at lowered and elevated temperatures as well as under illumination are easily implemented and frequently

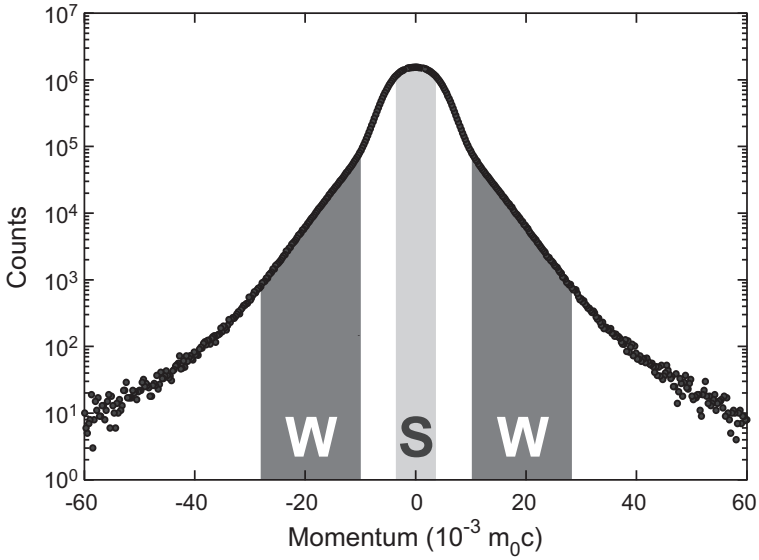

Figure 2.3: The S and W parameters are calculated from the Doppler spectrum to represent the proportions of valence and core electron annihilations.

used. With these measurements one can get more information about the nature of the defect, e.g. its charge state and the positron binding energy [6].

2.2 Positron lifetime beam techniques

The development of positron lifetime beams has been driven by the interest in several new epitaxially grown semiconductor materials and the absence of thick bulk samples. Also many problems in semiconductor physics are related to thin layers at interfaces. To investigate such samples with positron spectroscopy, fast positrons emitted from the source must be slowed down to monoenergetic before implantation into the sample. This is often done by thermalizing the positrons in a solid transmission moderator and then accelerating them to the desired energy. In the moderator, thermalized positrons can diffuse to the surface and be re-emitted due to a negative positron work function. Unfortunately only a very small portion of the initial positrons will thermalize in a moderator foil, the majority getting through as high energy particles. In tungsten, which is widely used as a moderator material, efficiencies in the range of $\sim 3 \times 10^{-4}$ are obtained in transmission configuration [7–10]. The inefficiency of the moderators necessitates the use of relatively high-active positron sources ~50 mCi in order to reduce the measurement time. The emission rate of the e^+ emission photons is so high and the

positron time-of-flight through the beamline so long ($\sim$1 μs with a wide spread) that the emission photon can not be used as a start signal of a measurement. In addition, it is in practice impossible to take into account the time distribution of the thermalization and re-emission process in the moderator.

In alternative lifetime measurement methods, the lack of the emission photon has been substituted e.g. by accurate release of a positron from a Penning-trap [11] or with the detection of secondary electrons emitted when a positron hits the sample [12]. In the latter method the time resolution is poor due to the difficulties in secondary electron detection. Better results have been obtained from the pulsed positron lifetime beams [1, 2, 13]. Pulsing of a monoenergetic positron flux is realized by longitudinal oscillating electric fields. The positron arrival time to the sample is correlated to the pulsing signal, which can thus be used in the measurement of the positron lifetime. The positron lifetime beam studied in this thesis is based on this pulsing concept, which is more closely presented in the next section.

2.3 TKK positron lifetime beam

The variable energy pulsed slow positron beam at the Helsinki University of Technology is designed for the positron lifetime measurements in semiconductors. For this purpose the positron lifetime beam must have a time resolution of the same order as positron lifetime in semiconductors, which is typically $>$150 ps. Additionally the measurement times should be practical, i.e. few hours per spectrum. This requires high efficiency of the moderator, the pulsing system and the annihilation photon detector.

2.3.1 Description of operation

Fast positrons are emitted from a ^{22}Na source (activity $\sim$50 mCi) and slowed down in a 1 μm thick tungsten single crystal (100) transmission moderator. The non-thermalized positrons are removed from the beam in a velocity selector, consisting of two solenoids arranged perpendicular to each other, see Fig. 2.4 where an illustration of the lifetime beam is shown. The remaining slow positrons are magnetically guided using solenoids and Helmholtz-coils. This monoenergetic slow positron beam is pulsed in a three-stage system consisting of a prebuncher, a chopper and a main buncher [14]. A schematic figure of the lifetime beam is presented in Fig. 2.5.

The prebuncher is needed to improve the efficiency of the pulsing system. It collects positrons into the time window of the chopper ($\sim$2 ns) avoiding unnecessary

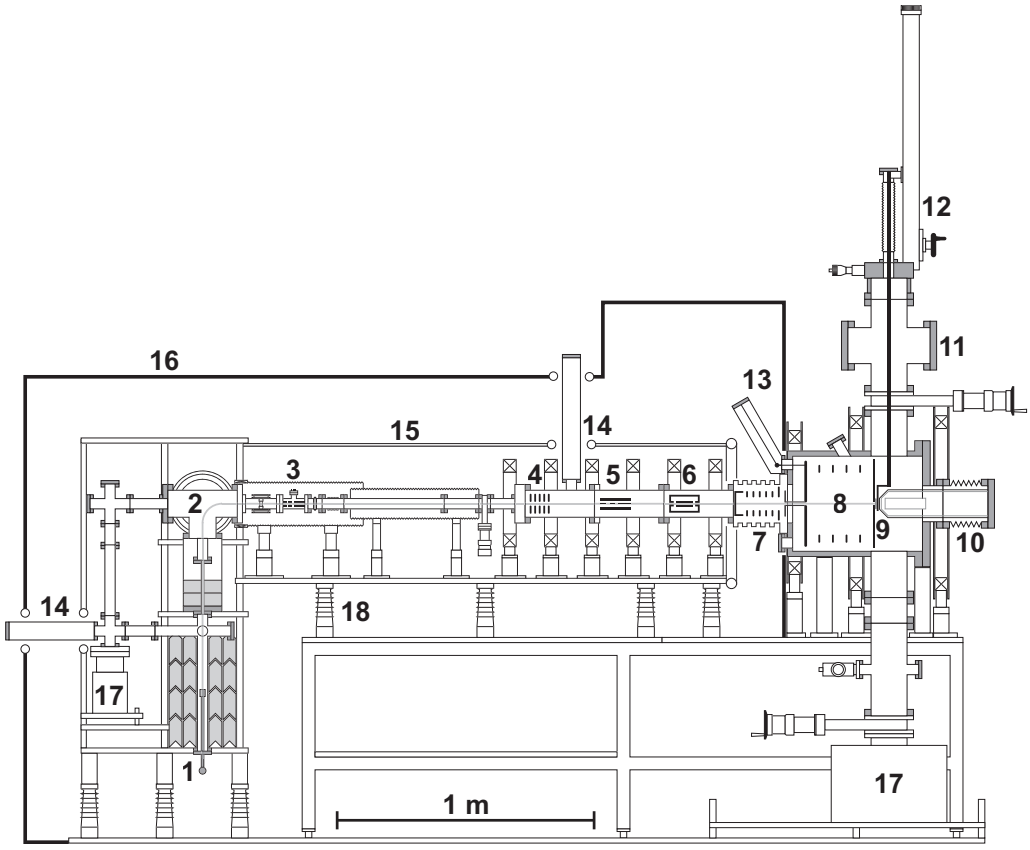

Figure 2.4: The schematical drawing of the positron lifetime beam in planned final configuration. 1. Positron source and moderator, 2. velocity selector, 3. pre-buncher, 4. pre-accelerator, 5. chopper, 6. buncher, 7. accelerator , 8. decelerator, 9. sample holder, 10. detector well, 11. pre-chamber, 12. room-temperature manipulator (to be installed), 13. HV-feedthrough, 14. pumping-line feedthroughs, 15. inner Faraday cage, 16. outer Faraday cage, 17. ion pumps, 18. stand-off insulator.

increase in the velocity dispersion of positrons, which degrades the time resolution of the system. The pulsing RF-signal of the double gap prebuncher is a combination of two sinusoidal signals at frequencies of 33 MHz and 66 MHz approximating the ideal parabolical pulsing signal [15]. It is produced by a waveform generator which allows the adjustment of signal phase and amplitude [16]. The pulsing signal is amplified with a 5 W RF-amplifier (Mini-Circuits ZHL-5W-1SMA) [17].

The positrons compress into pulses during the flight through a drift tube, which is followed by a 1 keV preaccelerator. The accelerated positrons enter the chopper which removes the background between prebunched pulses. This improves the

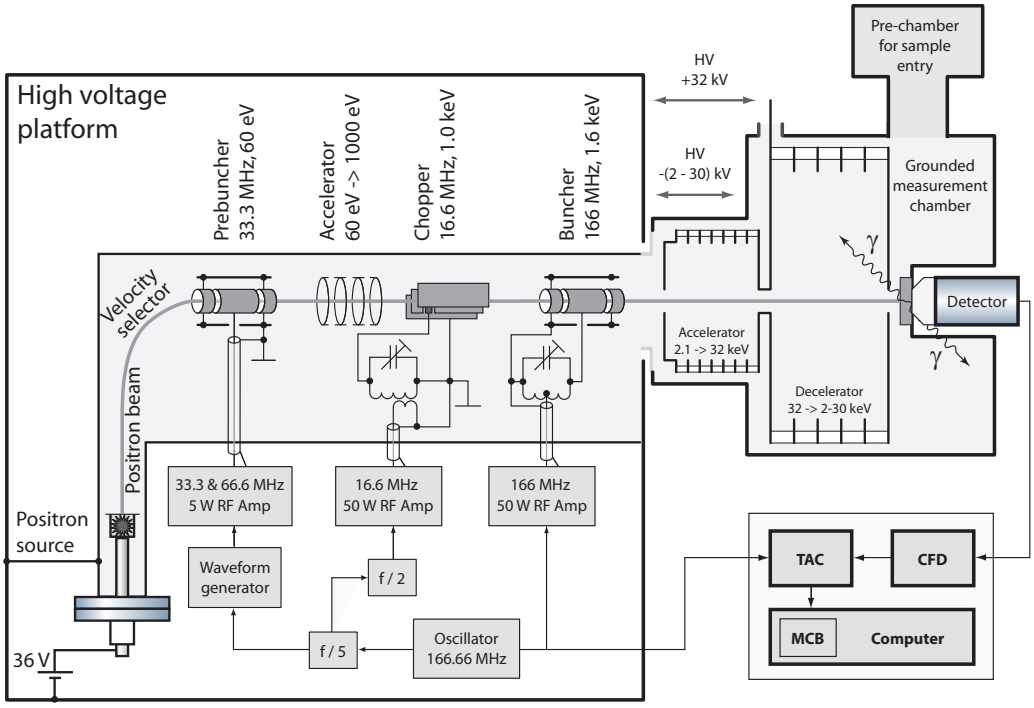

Figure 2.5: Schematic description of the operation of the TKK positron lifetime beam.

peak-to-background ratio of the time-resolution function. The chopper consists of a narrow slit with a thin deflection electrode located at the entrance in mid-gap, parallel to the walls. An oscillating transverse electric field is generated by the 16.6 MHz sinusoidal voltage connected to the deflection electrode. The chopper lets through the positrons arriving within a narrow time-window (∼2 ns). Outside the time window the deflection field is non-zero, radius of Larmor precession is increased and thus positrons collide with chopper walls and either annihilate or scatter. The walls are sawtooth shaped (see, Fig. 1 in Publ. I) in order to reduce the scattering of deflected positrons in the forward direction of beam. A correctly timed chopping signal with sufficient amplitude is generated by a pulsing circuitry with amplitude control and a high-power (50 W) RF-amplifier (Mini-Circuits LZY-1-SMA).

The final pulsing is done by the double-gap buncher. A sinusoidal signal at the frequency of 166 MHz is fed to the middle electrode, to produce the bunching electric fields. The middle electrode is part of an LC-resonance circuit, whose resonant frequency can be adjusted. The phase of the pulsing signal is adjusted to match the pulsing with the incoming pulse. A high-power (50 W) RF-amplifier (Mini-Circuits LZY-1-SMA) is used to amplify the signal for matched buncher.

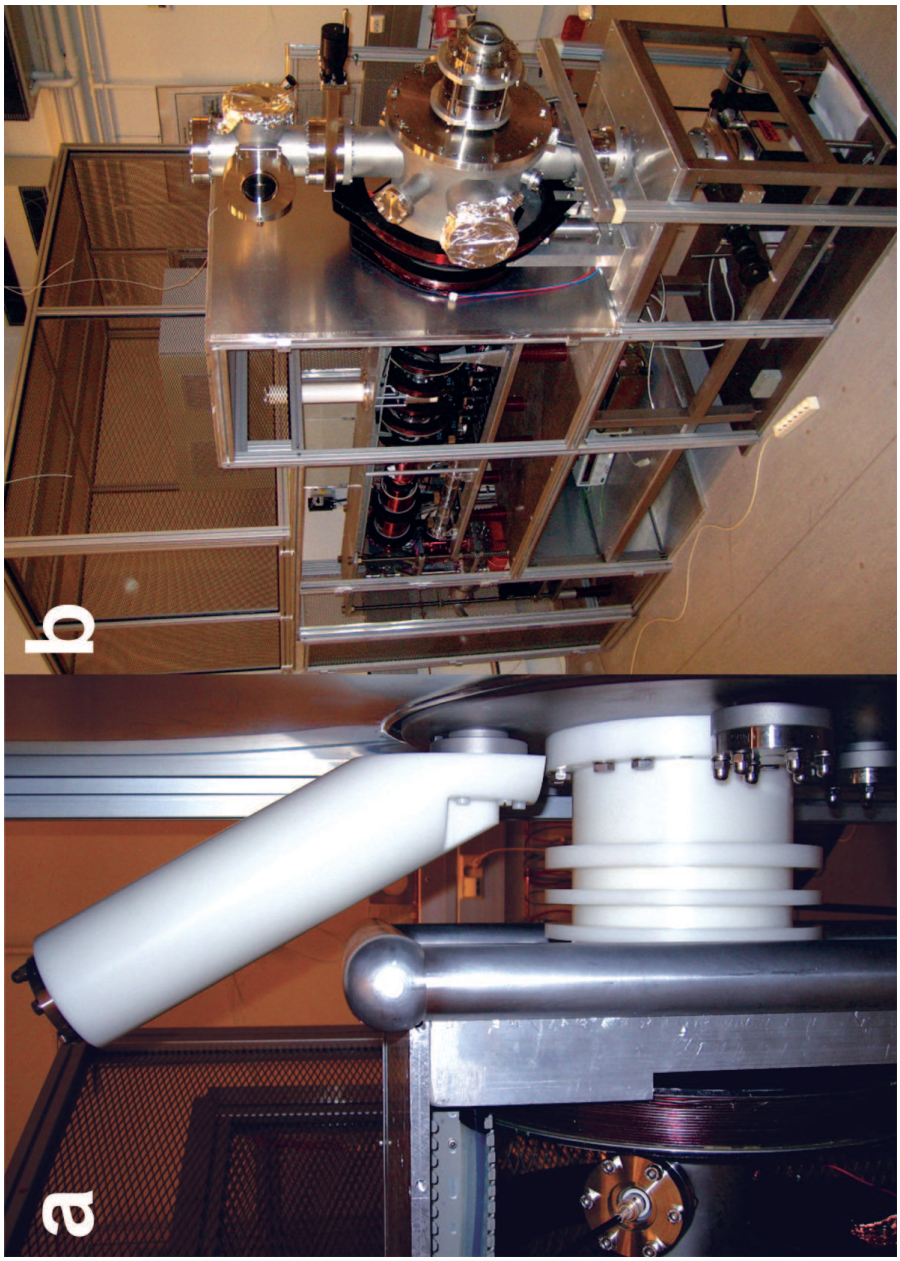

Figure 2.6: a) The lifetime beam without the measurement electronics and manipulators. b) The insulator between the HV-beamline and the grounded measurement chamber. The electrical feedthrough for the accelerating voltage is pointing upper-left.

The accelerator of this lifetime beam is an accelerator-decelerator structure with the aim of reducing the contribution of backscattered positrons in a lifetime spectrum. Also, the time-of-flight differences between different positron implantation energies is reduced by the increased average velocity of the positrons. The time-of-flight difference between the final positron energies of 2 keV and 30 keV is reduced from 9 ns to 1.5 ns due to this design [18]. The positrons are first accelerated to the fixed energy of 32 keV and then decelerated down to the final energy, which can be varied between 2 keV and 30 keV. The structure of the accelerator-decelerator is presented more closely in Sect. 3.3.2. The accelerator is located inside an insulator between the beamline and the main chamber (see Fig. 2.6 b) and the decelerator is in the measurement chamber. The size of the chamber has been chosen to allow increased diameters of the decelerator electrode rings, which makes the electric field more homogeneous at the beam axis. The design also helps to reduce the problems from back-scattered positrons.

Two XYZ-translators will be used as sample holders: one for the room temperature and other for the variable-temperature measurements between 20 K and 800 K. The changing of the room temperature sample holder is simplified by the use of a pre-chamber, enabling sample changing without breaking the main chamber vacuum. Measurement position of the samples is in the narrow gap between the last decelerator electrode and the detector well, where a BaF_2 scintillation detector is located. The BaF_2 crystal is used due to its detection efficiency.

A more detailed description and related discussion of the pulsing concept of the lifetime beam is presented in Ref. [15].

2.3.2 Timing properties - current status

It is practical to have a high detector count rate during the determination of timing properties of the pulsing components. To achieve this, the positron source was replaced with an electron gun (BaO cathode, ES-015 [19]) and a fast microchannel plate (MCP, Hamamatsu F4655-12 [20]) was used for the observation of the electrons. In addition to a high emission rate of electrons, the emission area (ϕ=0.8 mm) was significantly smaller than the area of the positron source (ϕ=4 mm). This improves the beam quality. Also, electrons emitted from a BaO cathode have a smaller energy spread (0.3 eV) than the moderated positrons ($\sim$1 eV). The MCP is capable of detecting single electrons and positrons with a good time resolution $\sim$100 ps.

In Publ. I the performances of the pulsing components were tested individually and in different combinations. The measured time resolution spectra, are shown in Fig. 2.7. The spectrum obtained with the prebuncher was not ideal showing strong asymmetry (curve 1) and the full width at half maximum (FWHM) 3.1 ns. The

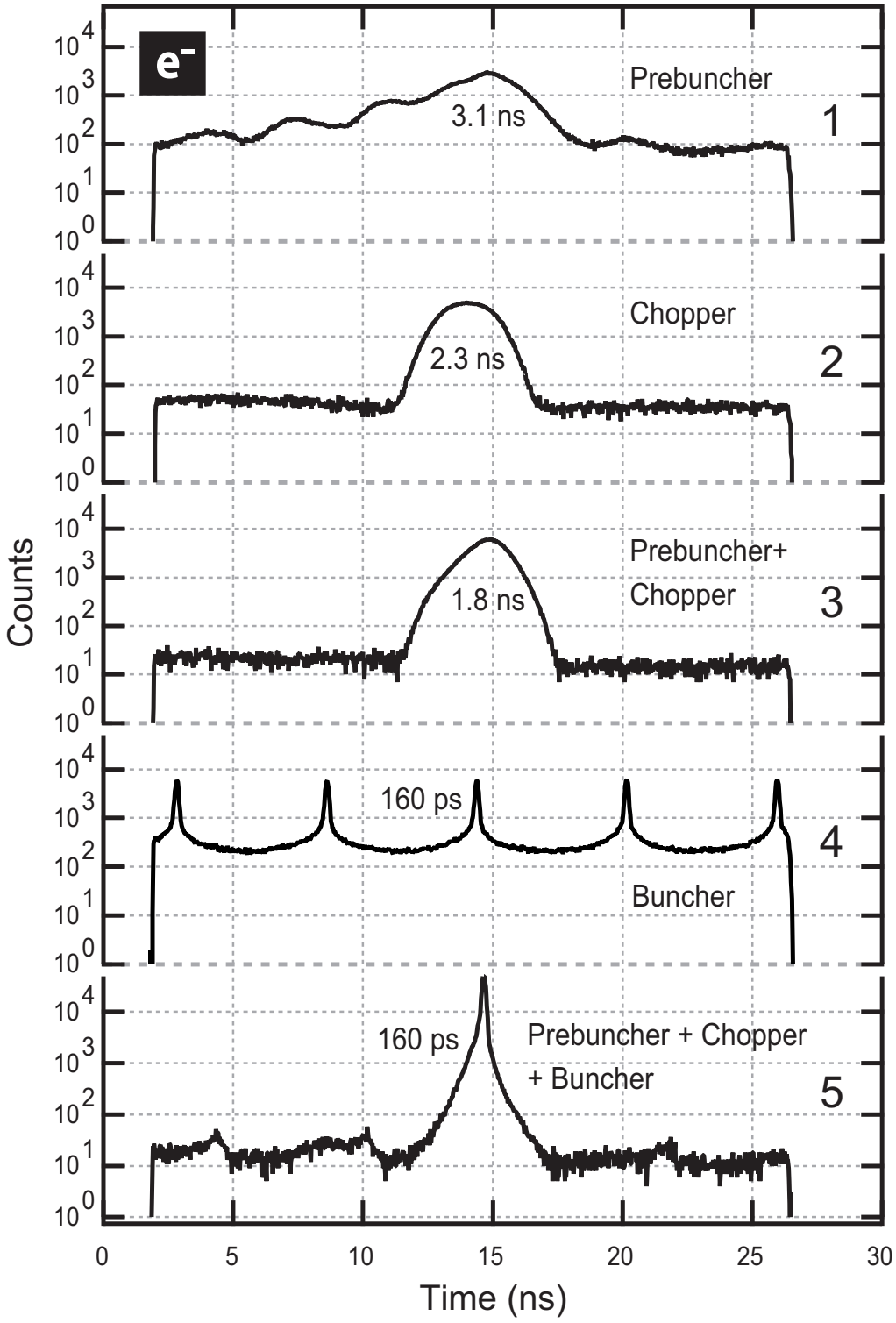

Figure 2.7: The time resolution spectra measured with different pulsing components. The FWHM values for each spectrum are shown.

chopper produced a spectrum with a flat background and a symmetric peak with FWHM of 2.3 ns and P/B ratio of 100 (curve 2). When using the prebuncher with the chopper, the P/B increased to 300 and the FWHM decreased to 1.8 ns (curve 3). The buncher proved to operate properly as it produced a spectrum (curve 4) equal to the ideal spectrum observed in simulations of sinusoidal bunching [21]. The FWHM of a single peak was 160 ps and P/B approximately 30. All the pulsing components working in sequence produced a time resolution of 160 ps with a peak-to-background ratio of 5000 (curve 5).

Several unpublished pulsing tests have been carried out with positrons using an MCP as a detector. To give an idea of the present status of the lifetime beam the FWHM and peak-to-background values obtained from latest tests have been shown in Table 2.1. The most remarkable result of these tests was obtained with positrons using all the pulsing components. The observed time resolution was 170 ps and the peak-to-background ratio more than 1000 [21], which is enough for positron lifetime measurements in semiconductor materials.

As a demonstration, the lifetime of positrons annihilating in the MCP was measured (Fig. 2.8) using a BaF_2 scintillation detector. Because of the non-optimal measurement arrangement, the MCP was used to produce gating pulses for the scintillation detector pulses in order to enhance the P/B ratio. A P/B ratio of 200 was observed and the bunchers side peaks can be seen on both sides of the main peak, 6 ns away.

Table 2.1: The FWHM and peak-to-background ratios of the optimized time resolution spectra produced by the pulsing components. Some of the spectra are presented in Refs. [15, 21].

	Electron tests		Positron tests	
Pulsing component	FWHM	P/B	FWHM	P/B
Prebuncher	3.1 ns	30	5 ns	7
Chopper	2.3 ns	∼100	1.5 ns	150
Buncher	160 ps	30	200 ps	20
All in sequence	160 ps	∼5000	170 ps	>1000

Publication II focuses on the improvements made to the chopper design. In the first pulsing tests of the chopper, a poor time resolution of ∼8 ns was obtained [22]. The performance was improved simply by increasing the chopping power by a high-power RF amplifier. The improvement was clear in terms of FWHM (∼2.5 ns) but an unacceptable highly asymmetric background was observed. The anomaly in the background was interpreted to be a consequence of the scattering of electrons inside the chopper. With the 'sawtooth' design, the scattering of electrons (and positrons) in the forward direction of the beam was prevented.

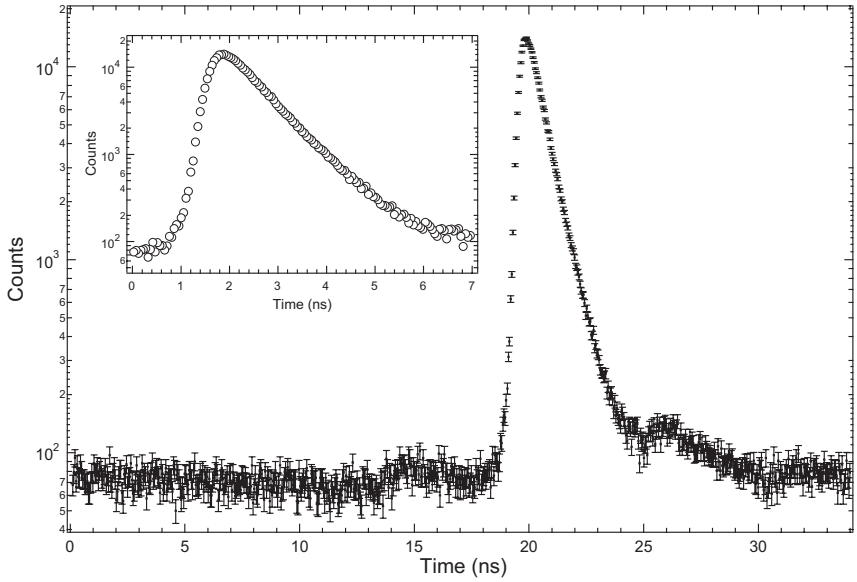

Figure 2.8: The lifetime spectrum of positrons annihilating in the microchannel plate measured with a BaF_2 scintillation detector.

Chapter 3

High-voltage design of the positron lifetime beam

The aim of this thesis was to design and test a reliable high-voltage construction for the positron lifetime beam. This aspect of the beam is discussed in this chapter, which refers to Publs. III and IV. The unique property of the TKK lifetime beam is the grounded sample, which simplifies the sample manipulation, i.e. moving, heating, cooling, biasing and illumination. The challenge of this concept is that the rest of the equipment, including most of the electronics, must be floated at high potential for positron acceleration. This requires large protective installations around the beam to keep users safe. In addition, attention must be paid on the transient protection of electrical components at high potential. All the mechanical parts have to be designed to minimize the risk of an electrical breakdown, which can induce destructive surge currents. To be on the safe side, all electrical devices at high potential are individually protected against these currents.

The high voltages at the accelerator-decelerator electrodes and the limited space around them require careful design to avoid discharges despite the higher breakdown strength of vacuum compared to air. The design and the choices of materials for solid insulators between the electrodes are important in discharge elimination.

3.1 Discharge mechanisms

If the electric field strength locally exceeds the breakdown field strength of an insulator, a discharge occurs. When the discharge channel extends through the whole insulator and insulation capability is totally lost, one speaks of a complete

breakdown. If a discharge occurs along a surface it is called flash-over. Usually in uniform or quasi-uniform field gaps the breakdowns occur as complete breakdowns. The sufficient dimensions of the gaps can be determined with help of Paschen's curve [23], which gives the breakdown field strength as a function of the product pd of the gas pressure and the electrode distance.

In practice, breakdowns usually start at sharp edges of an electrode, where the electric field is highly non-uniform and the breakdown field strength is locally exceeded. The reduction in breakdown field strength due to field enhancement is described with Schwaiger's factor $\eta = E_{\mathrm{mean}}/E_{\mathrm{max}}$ [24]. $E_{\mathrm{mean}} = V/d$, where V is potential difference between two electrodes and d is a shortest distance between them. E_{max} is the maximum electric field strength in the gap. This enhancement of the field strength plays an important role in high-voltage design. Highly non-uniform electric fields must be eliminated by field stress controllers, such as corona rings, to prevent discharges.

In highly non-uniform fields smaller discharges are observed long before a complete breakdown occurs. These incomplete discharges may be transient or steady state, and the discharge channel will not bridge the whole insulation. Partial discharges (PD) are examples of an incomplete discharge. They are localized electrical discharges that only partially bridge the insulation between conductors [25]. Partial discharges can take place on the surfaces of conductors or inside cavities of an insulator. On account of their importance, PDs are discussed in more detail in Sect. 3.1.2.

Breakdowns are always harmful. The temperature rises very high near the breakdown channel due to the high current flowing through it. In solids this is destructive as the material can not restore the degradation of the insulator near the discharge channel, unlike gaseous insulator materials which are self-restoring and permanent degradation of the insulation is not incurred. Breakdowns also induce surge currents, and depending on the energy, these can present a considerable risk for the devices connected to the system. Therefore, devices in the lifetime beam are protected against these surge currents. Transient suppression techniques are discussed in Sect. 3.4.

3.1.1 Breakdowns in vacuum

Because the breakdown field strength of high-vacuum, ~90 kV for 1 mm gap and ~160 kV for 5 mm gap [26], is so high, breakdowns in vacuum are usually initiated through generation of an ionizable medium at the gap under high electric field stress. This can be a consequence of vaporization or melting at the electrode surfaces. In a 'cathode initiated breakdown' a microprotrusion is vaporized due to the field electron emission (FEE) current [27] flowing through it. At the anode,

melting process can be initiated by electron bombardment, which causes the metal vapor pressure to become high enough for the onset of a breakdown ('anode initiated breakdown').

3.1.2 Partial discharges

Partial discharges are the most important degradation mechanism in the deterioration of insulator materials, especially polymer materials. PDs can take place inside an insulator at defects where the dielectric strength is locally reduced. Usually PDs initiate at gas-filled voids or metallic particles remaining in the material. The destructive behavior of PDs is based on a phenomenon called electrical treeing, where gas-filled channels are created gradually from electrode to electrode [28]. Currents can flow through these thin channels, which get wider until a complete breakdown occurs between the electrodes and the insulator is totally deteriorated [29].

Partial discharges have to be taken into account especially in AC systems where PDs are ignited on every voltage cycle and the treeing process is accelerated. With DC-voltages PDs occur usually only when raising or lowering the voltages over the insulator.

A partial discharge can also take place in a gaseous insulator on the surface of a conductor. Then it is called corona. These discharges can be eliminated by keeping the conductor system free of sharp edges and protrusions. Corona discharges emit electromagnetic radiation at radio frequencies which can interfere with sensitive measurement electronics.

In the lifetime beam, partial discharges must be taken into account in the most critical insulator structures located between the electrodes in the accelerator and the decelerator. The accelerator-decelerator was tested for partial discharges, the measurement setup and results are presented in Sect. 3.5.1.

3.2 High-voltage floating of the beam

3.2.1 Floating of the beamline

The entire vacuum system, excluding the main measurement chamber, is floated at an adjustable potential between 2 kV and 30 kV for positron acceleration. The beamline with the guiding magnets is enclosed inside a Faraday cage. The HV-enclosure comprising the control electronics is connected to the inner Faraday cage, forming the HV-platform (Fig. 3.1). Another grounded Faraday cage is built

around the inner one to protect users and to guarantee that the electric fields are clearly confined and well-defined. This helps to avoid discharges between the high voltage parts and the ground. Additionally, the cages act as electromagnetic shields, bounding the radio frequency emission induced by the pulsing electronics.

The HV-platform is kept at high potential with a HV-power supply (U_1 in Fig. 3.1), whose voltage is adjustable between 2 kV and 30 kV. A floating power supply (U_2), located inside the HV-enclosure, is used to produce a constant voltage (-32 kV) for the accelerator. The voltage is connected to the middle electrode between the accelerator and the decelerator. Since U_2 is higher than U_1, the potential of the middle electrode is always negative and the positrons are slowed down as they travel through the decelerator to the ground potential. A positron energy-level diagram of the lifetime beam is sketched in Fig. 3.2.

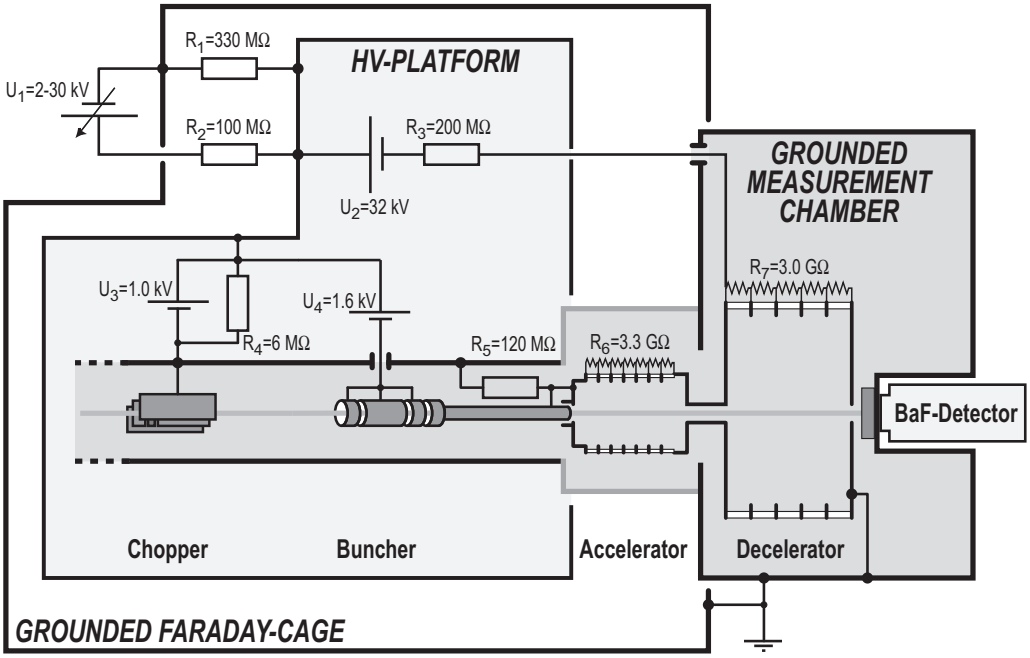

Figure 3.1: A diagram of the circuit used to float the lifetime beam at the HV. The sourcing-only properties of the HV-power supplies and the accelerator-decelerator structure give rise to the complexity of the circuit. The source area, the pre-buncher and the pre-accelerator are not shown.

3.2.2 Floating of the HV-supplies and control electronics

All the HV-power supplies are switched-mode power supplies and therefore they cannot be used as current sinks. This necessitates the use of by-pass resistors (R_1

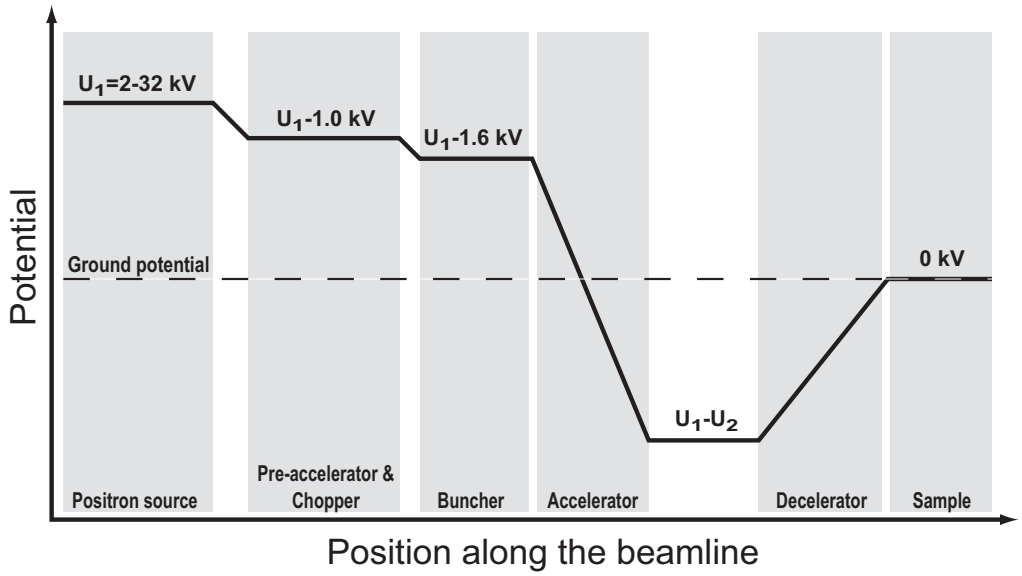

Figure 3.2: The potentials in the lifetime beam along the beamline. The positron end energy is defined by the adjustable high-voltage power supply (U_1).

and R_4). Additional load resistors (R_2 and R_3) help to limit the peak currents if a breakdown occurs. This reduces the degradation of electronics and insulators in the system as well as the HV-power supply itself. The load resistors made of special high voltage resistors [30]. Due to the limited power dissipation capability (1 W) and the maximum voltage (10 kV) of a single resistor, air-insulated resistor chains were constructed. These chains were placed inside acrylic tubes.

The power needed for at the HV-platform is 3 kW at the maximum. For transmission of power from the ground potential to high potential, a high-voltage DC isolation transformer is needed. For this purpose an epoxy encapsulated single-phase transformer (RUBY SERIES IT100-5E-J-AT) [31] is used. It is rated to withstand a potential difference of 100 kV(DC) between primary (230 V(AC)) and secondary (230 V(AC)) and to supply 5 kVA power to high potential.

3.2.3 Floating of the pulsing components

Two power supplies (U_3 and U_4 in Fig. 3.1) are used for generation of pre-acceleration voltages ($<$2 kV). The pre-accelerator and the chopper are at a potential of -1.0 kV and the buncher at -1.6 kV relative to the HV-platform. The exit-tube of the buncher is connected to the voltage divider chain of the accelerator and its potential relative to the HV-platform potential is -2.1 kV, when U_2 is -32 kV.

Double DC-blocks needed in the RF supply lines to HV floating pulsing components are introduced in Sect. 3.6.

3.3 The design of the high-voltage parts

The high operating voltages must be taken into account in the mechanical design of the Faraday cages, vacuum feedthroughs, electrical feedthroughs and particularly in the accelerator-decelerator structure. A finite element analysis program *QuickField* [32] was used to simulate electric fields in the system and the results were used when the beam parts were designed.

3.3.1 Faraday cages

The designing of the cages had to be done carefully to ensure that they are HV-proof. Firstly, the separation distance between the cages has to be adequate to ensure low enough electric-field strength. Secondly, all the corners and edges of the inner cage should be rounded with a sufficient radius of curvature to prevent field enhancement. Thirdly, inside the cage sharp shapes are eliminated to avoid corona discharges.

The insulation of the inner Faraday cage is realized by stand-off insulators (Fig. 2.4 item no. 18), otherwise it is air-insulated from the outer cage. The air gap between the cages is at minimum 140 mm. The most critical, i.e. shortest separation between the cages is at the end of the beamline tube. Extra roundings have been added there at the edges of the inner cage (Fig. 2.6 b).

3.3.2 Accelerator-decelerator

The high voltage design of the accelerator-decelerator focuses on the shaping of the electrodes and insulators as well as on the material choices and finishing of the electrodes.

The accelerator (item no. 7 in Fig. 2.4) consists of eight electrode rings and the decelerator (item no. 8) of six rings. The mechanical support for the electrodes is made of polyoxymethylene (POM, also known as polyacetal, commercial name Delrin) rods and spacers. POM has a dielectric strength of 20 kV/mm [33], it is easily machinable and it has good mechanical properties. The accelerating and decelerating potentials are distributed to the electrodes by resistive voltage-dividers. The resistors used are high-precision, non-magnetic, vacuum compatible

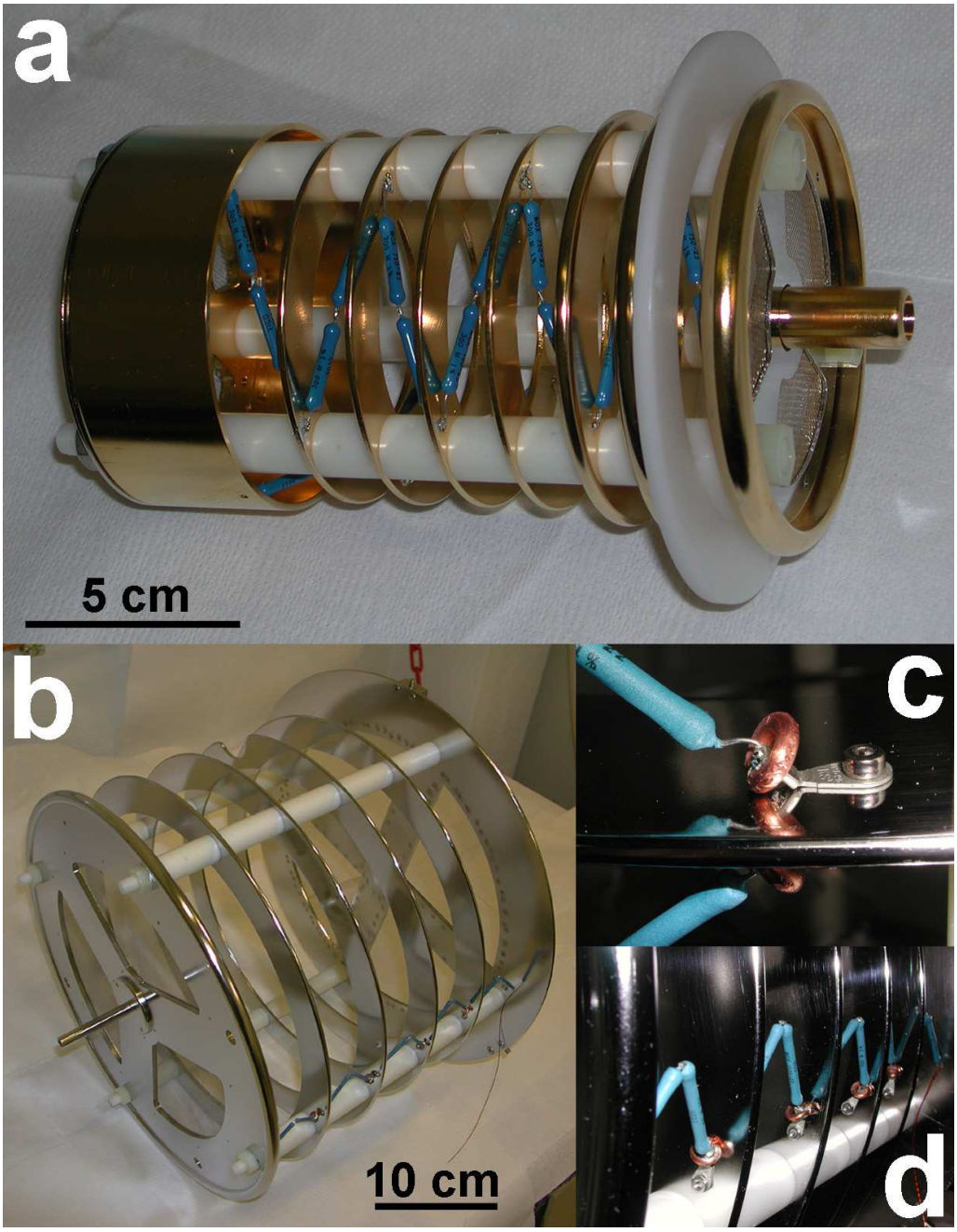

Figure 3.3: a) The accelerator and b-d) the decelerator. c) Miniature corona rings used at the mounting clip of the HV-resistors.

high voltage resistors (MOX-1125-22 and MOX-750-23) [34]. Photographs of the accelerator and the decelerator and shown in Fig. 3.3.

The accelerator is located inside the insulator structure made of POM. The space is restricted in all directions which makes the design more challenging because of the requirements for the electrode diameters to get a homogeneous accelerating electric field on the beam axis. The design of the decelerator is more straightforward due to larger space for it. Reasonable values for the radius of curvature of the electrode edge and for the gap between the electrode and the insulator or chamber wall were found by simulations.

A result from a simulation of the electric field in the accelerator is shown in Fig. 3.4. The last electrode of the accelerator has a very large radius of curvature at its edge to keep the field enhancement small.

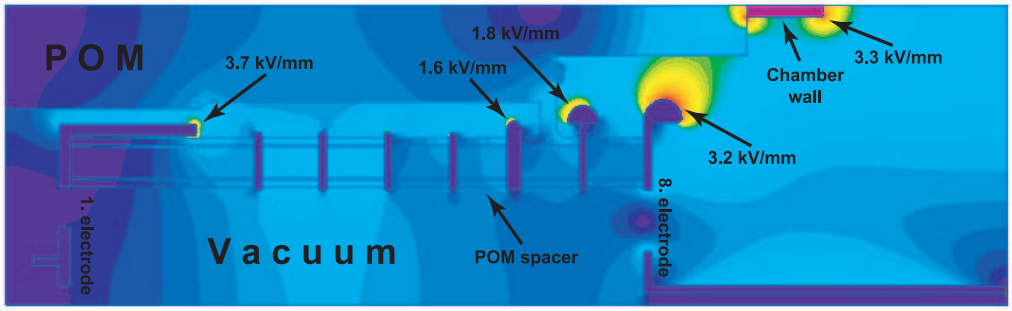

Figure 3.4: The simulated electric fields in the accelerator. Electric field strengths are shown at critical locations.

By choosing the correct material for the electrode one can enhance the breakdown strength of the vacuum gap. Stable high voltage electrode materials for UHV applications are e.g. titanium, stainless steel and molybdenum [27]. Electrodes for the main accelerator were made of non-magnetic (AISI 304) stainless steel, because of its machinability, availability and low cost. The electrodes were chemically polished to eliminate sharp protrusions on the surface. The electrodes of the accelerator were also gold plated, which made the surface even smoother and allowed soldering of the HV-resistors onto the electrodes.

3.3.3 Pumping line feedthroughs

The vacuum in the beamline is created by pumping through the accelerator and through two pumping lines are as indicated in Fig. 2.4. To avoid floating of turbo-pumps at high voltage, pumping is done through isolated pumping line

feedthroughs made of POM. The challenge with these feedthroughs is the prevention of the surface flashovers because of the lower breakdown strength of surfaces. Surface discharges ignite almost at a constant voltage, depending only slightly on the length of the insulator [26]. Because of this, the endings of the feedthroughs have to be formed so that the parallel electric field strength can not rise near the surface of the insulator. When the feedthrough is connected to a standard CF vacuum flange floating at high potential, the enhanced electric field at the unrounded edges of the flange will generate high electric fields parallel to the surface of the insulator (Fig. 3.5). To prevent surface discharges corona rings have been utilized to smooth down the electric field distributions. A big safety factor must be used due to the lowering of the breakdown strength as the surface of the feedthrough gets contaminated with time.

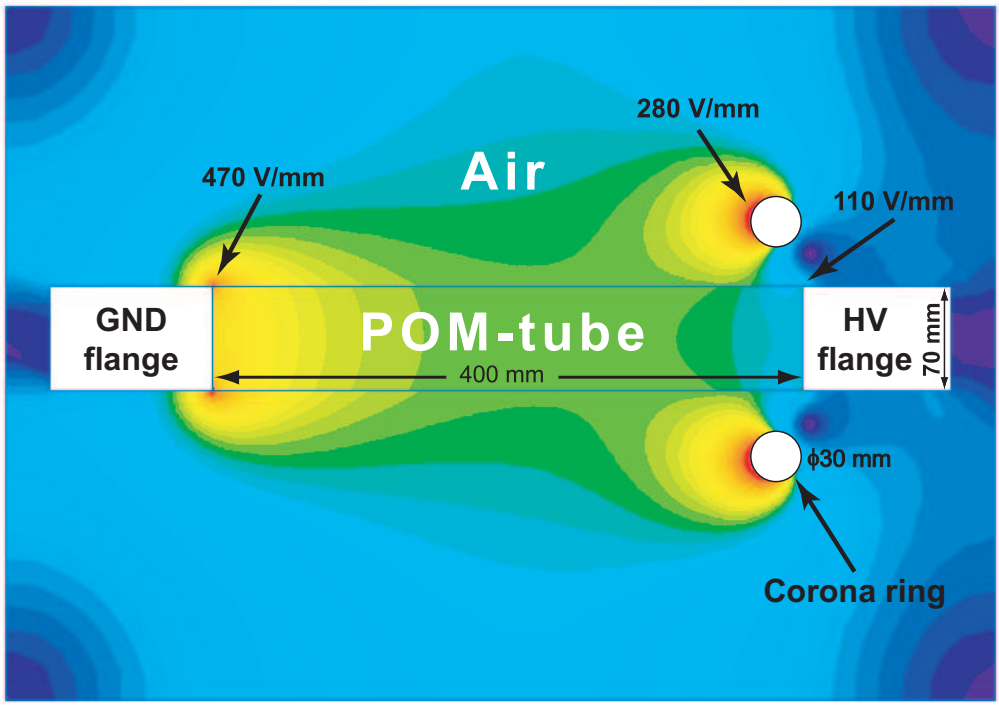

Figure 3.5: An electric field simulation of an isolated pumping line. Highly non-uniform electric fields are generated near the unrounded edges of the flange at the surface of an insulator (on the left in the picture). With a corona ring the enhancing of the electric field can be prevented (right).

QuickField was also used to simulate the electric fields around the pumping feedthrough. In the simulation a corona ring at the right end of the feedthrough was included. The electric fields generated at grounded and high voltage flanges

would be equal without the corona ring, so the real difference can be seen from the results (Fig. 3.5). The Schwaiger's factor (η) describing the breakdown strength was 0.21 without the corona ring, and is increased to 0.91, i.e. by more than factor of four, when the corona ring is used. The field enhancement at the surface of the corona ring is not a problem due to the higher insulation strength of air.

3.3.4 Double DC-blocks

A double DC-block is a component which isolates the DC-voltages over its terminals but lets AC signal through. 'Double' stands for the isolation of both the inner and outer conductors of the coaxial cable. The isolation is done with porcelain high RF-power multilayer capacitors [35], which have a high Q-value (>10000) and voltage rating of 2.5 – 3.6 kV. The outer conductor is blocked with three surface-mount capacitors and the inner with one. The coaxially arranged capacitor system is enclosed inside an RF-proof can in order to prevent interference with other RF-electronics. The can consists of two aluminum cups which overlap each other and POM insulator in between. A DC-block is shown in Fig. 3.6.

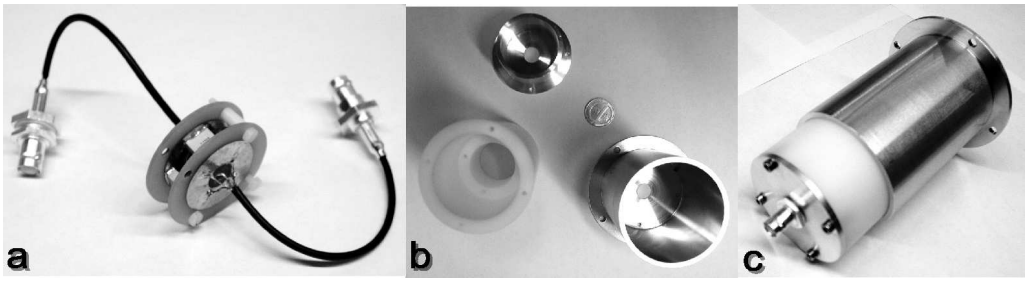

Figure 3.6: The DC voltage component is blocked from the pulsing RF-signals with the double DC blocks. a) The capacitive element, b) RF proof can and the isolator, c) the completed DC block.

3.4 Overvoltages and surge protection

An overvoltage is a voltage which exceeds the long-term nominal voltage designed for a device. The most important criteria in categorizing overvoltages is the duration of the front edge of a pulse. Four different categories are used [36]:

- Temporary overvoltages (>10 ms)
- Slow-front overvoltages (~0.2 ms)

- Fast-front overvoltages ($\sim$1 μs)
- Very-fast-front overvoltages ($<$100 ns)

In this work we focus on the fast-front and very-fast-front overvoltages as they are induced by discharges, which are the most probable malfunctions in our equipment.

The very short leading edge and duration of transients makes them difficult to be protected against. Transients are generated usually when an electrostatic charge is discharged rapidly, e.g. by a breakdown, or by electro-magnetic induction. A high amplitude transient causes breakdowns or short circuits in devices, but in the end it is the energy of a transient pulse that destroys a device. Transients are a very common cause for failures, but there are ways to protect against them.

The propagation of the transient pulses is determined by the transfer line properties of the system. The pulses can be reflected from interfaces of two transfer lines with different characteristic impedances. The amplitude of a transient can multiply significantly by piling-up, especially in a relatively small systems where the pulse length is much longer than the propagation time through the system (such as in the case of Faraday cages of the lifetime beam). This may cause unexpected insulation failures if the safety factors are too low.

Transients tend to head towards ground potential along the shortest way, but in addition they can spread inside a system by galvanic, capacitive or inductive coupling. This makes the prediction of propagation paths of transients very difficult. Therefore it is practical to protect all the electronic equipment from transients. A basic requirement in reduction of transient induced damages within a system is low impedance grounding, because the grounding impedance causes a potential rise when a transient current flows through it [37].

Due to the inductance of conductors the leading edge of a transient gets longer and amplitude smaller as it propagates. A rule of a thumb is that one meter (1 m) of a conductor corresponds to an inductance of one micro henry (1 μH). This smoothening of a pulse due to the inductance is used in the transient protection concepts (see next section).

3.4.1 Surge protection

The electronics in the lifetime beam, such as the power supplies and pulsing electronics must be protected against fast high voltage transients. The energy of a worst case transient can be estimated in the positron lifetime beam. The two nested Faraday cages form a capacitor and a breakdown of air between them creates the biggest possible current surge in the system. The capacitance is estimated

to be ∼0.5 nF and the pulse energy can then be calculated from the potential difference of the cages. A capacitance of the order of 0.5 nF and a voltage of 30 kV gives ∼0.3 J for the pulse energy. Also, the surge current can be estimated by a simple calculation: 0.5 nF capacitor charged to a potential of 30 kV carries a charge of 15 μC. If this is released during a time period of ∼10 ns, a surge current of 1500 A is produced. This is, of course, only an order of magnitude estimation, but it shows that we are not dealing with very high currents, such as in a thunderbolt (∼10 – 100 kA). This value can be used to select proper transient suppressors.

A variety of components have been developed for overvoltage protection. These are based on e.g. ionized gas breakdown, semiconductor junction breakdown or frequency dependent LC-filtering. They are used to reduce the overvoltage pulse energy to a level tolerable for the devices under protection by short circuiting the transient currents to the ground. The most common types of these components are spark gaps, gas discharge tubes (GDT), varistors and avalanche diodes. These can operate with both polarities and therefore they are usable with both AC and DC voltages. The important characteristics of transient suppressors are:

- Energy handling capability
- Impulse current dissipation capability
- Response time
- Residual voltage (protection level)
- Bandwidth

These properties vary for different components and one type usually can not offer sufficient protection alone. The differences between the components are often utilized in surge protection by combining different types into a multi-stage protector device (Fig. 3.7). In this concept, the first stage is a coarse protection done with a gas discharge tube or a spark gap, which have high peak current tolerance (∼30 kA). Gas discharge tubes are available over a wide variety of sparkover voltages. This is, however, a function of rise time, and for very-fast-front pulses it can increase by a factor of 10 from the nominal value.

A varistor can be used as a middle stage to further reduce the peak voltage. It is faster (response time less than 25 ns) than a GDT, but its energy dissipation capability and voltage limiting characteristics are still good (∼200 J, ∼8 kA) [38].

The third stage consists of a fine protector, e.g. an avalanche diode. This is a fast component with very accurate voltage limiting characteristics. The power

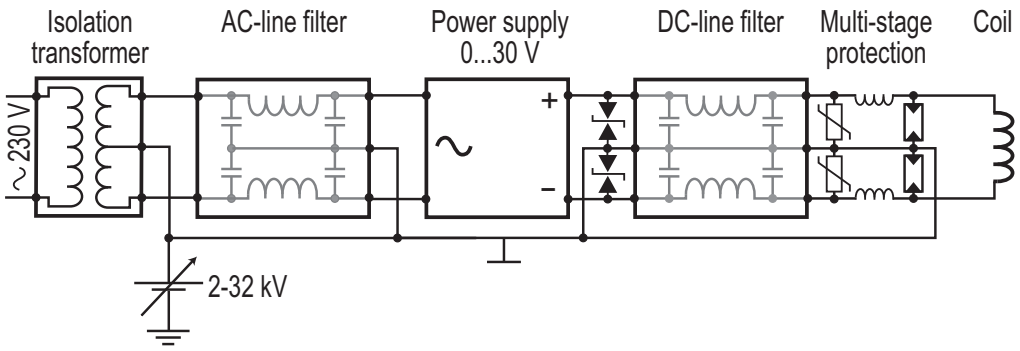

Figure 3.7: The multi-stage protector system used in the lifetime beam to protect power supplies from overvoltage transients. Isolation inductances are used between the protection stages to ensure the sequential operation of the protector components.

dissipation capability for a 1 μs transient is $\sim$0.2 J, so it is suited only in the filtering of low power transients.

The protection stages are separated by additional isolation inductances. These smoothen, i.e. reduce the rate of voltage rise and the amplitude of the propagating transient and make the protective components operate in sequence, which is required for efficient transient suppression and protection of the most sensitive components.

For the DC-power supplies we built multi-stage protectors where a GDT with a DC-sparkover voltage of 90 V is used as a first stage. For a transient with a voltage rise of 1 kV/μs the sparkover voltage is $<$600 V [39]. For the second stage, a varistor with a clamping voltage of 31 V and energy dissipation capability of 0.7 J was utilized [40]. We use an additional LC filtering stage between the varistor and avalanche diode stages. A commercial DC line filter made of capacitors and inductors is used as a low-pass filter. An avalanche diode with the breakdown voltage of 33 V was used as the last protection stage [41].

To protect the RF-amplifiers feeding the pulsing components, commercial military class suppressors are used (FCC-250B-230-BNC and FCC-550-20-BNC) [42]. These are extremely fast (clamping time 2 ns) suppressors designed to provide protection for sensitive semiconductor electronic circuitries. Transient energy is reduced to the sub-millijoule range. These protectors are matched to the pulsing signal frequencies (16.6 MHz, 33.3 MHz, 66.6 MHz and 166.6 MHz).

3.5 HV-withstand tests of the system

Different high-voltage parts of the lifetime beam were independently tested. The main accelerator, multi-stage transient suppressors, high-voltage load resistors and the HV-platform itself were tested to find the weakest points in the insulation and eventual design errors.

The HV withstand test for the main accelerator and the HV load resistors, as well as floating test for the HV-platform were done simply by connecting a DC high voltage over the insulation under investigation and monitoring the voltage and current outputs of the HV-power supply. A plotter was used in long-term ($\sim$1 week) tests to observe surges induced by the discharges.

The stability requirement for the accelerator voltage can be easily estimated. In practice time-of-flight spread should be less than one channel (10 ps) in the time resolution spectra. The total time-of-flight of a positron in the main accelerator is 14 ns. For the time spread

$$\frac{\Delta T}{T} = \frac{1}{2}\frac{\Delta E}{E}. \tag{3.1}$$

From this 40 V can be estimated for the maximum allowed drift or partial discharge induced voltage ripple at an acceleration voltage of $\sim$30 kV.

In the long-term tests, the load resistors and the insulation of the HV-platform were found to be high voltage proof. In the main accelerator tests (in vacuum), voltages of negative polarity were observed to induce small discharges at -40 kV at intervals of 1 hour. These discharges were interpreted as surface discharges at the electrode spacers, with low energy. Voltage dips were not observed below -35 kV, which is the voltage range where the main accelerator will be operated.

Due to the importance of voltage stability of the main accelerator in the formation of positron pulses and to the time resolution, additional PD-measurements were done using more sophisticated testing equipment. These tests are discussed in detail in Sect. 3.5.1. The transient suppressor performance test setup is described in Sect. 3.5.2.

3.5.1 Partial discharge measurements for the main accelerator

Partial discharge tests in the main accelerator were done both with simple DC measurements and with a more refined phase resolved AC method. In the phase resolved partial discharge (PRPD) method the device to be tested is stressed with

an AC high voltage. Since different types of discharges occur at characteristic polarities and phases of the sinusoidal excitation voltage, it is possible to discriminate between e.g. PD, corona and sparking due to bad electrical connections [43].

The measurement setup is depicted in Fig. 3.8. High voltage was applied to the middle electrode between the accelerator and the decelerator, so that both of them are tested at the same time. The 50 Hz alternating high voltage was produced from the mains voltage by a HV transformer. A 1 nF (C_1 in Fig. 3.8) capacitor was connected parallel with the main accelerator and a pulse transformer was used to measure the fast PD-induced pulses. A capacitive voltage divider, consisting of a 100 pF and a 100 nF capacitors (C_2 and C_3), was used to produce a reference AC signal for measurement of phase angle (time of occurrence) of PD-pulses. An oscilloscope was used to observe the partial discharge induced voltage peaks and the reference voltage for the PRPD measurements.

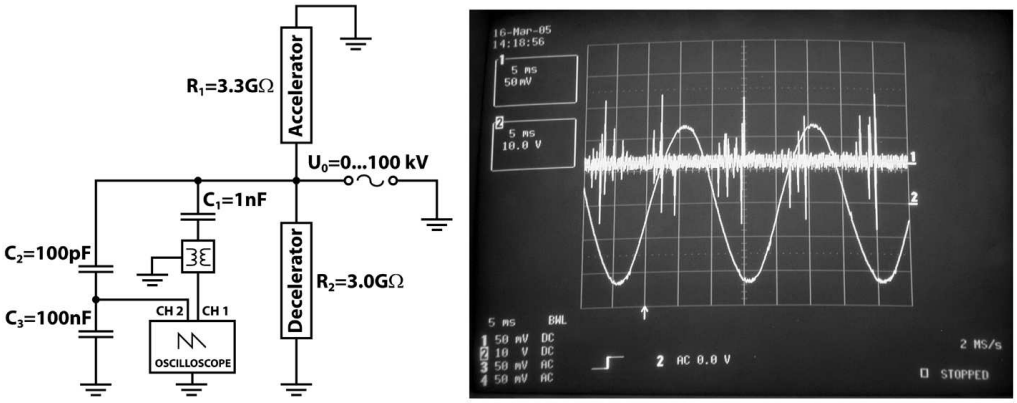

Figure 3.8: a) The measurement setup for the detection of partial discharges in the main accelerator. b) An oscilloscope reading for a PD measurement where internal partial discharges are observed.

Partial discharges in the main accelerator were observed in DC measurements. They appeared at voltages of 17 kV but died out after a while even at higher voltages (40 kV). With AC voltages partial discharges started as the peak voltage was raised to 27 kV. These discharges were observed at a phase of the voltage cycle (Fig. 3.8), which is characteristic of internal partial discharges [43].

3.5.2 Performance testing of transient suppressors

The surge currents for testing were produced by charging a HV cable (RG213/U) to high voltage and discharging it by a breakdown to the target. A ∼5 m long cable simulates the Faraday cage system of the lifetime beam with its 0.5 nF

capacitance and 25 ns propagation time. Thus both the energy and the shape of a test transient corresponds to the transient energy released by a complete breakdown of the HV insulation of the lifetime beam.

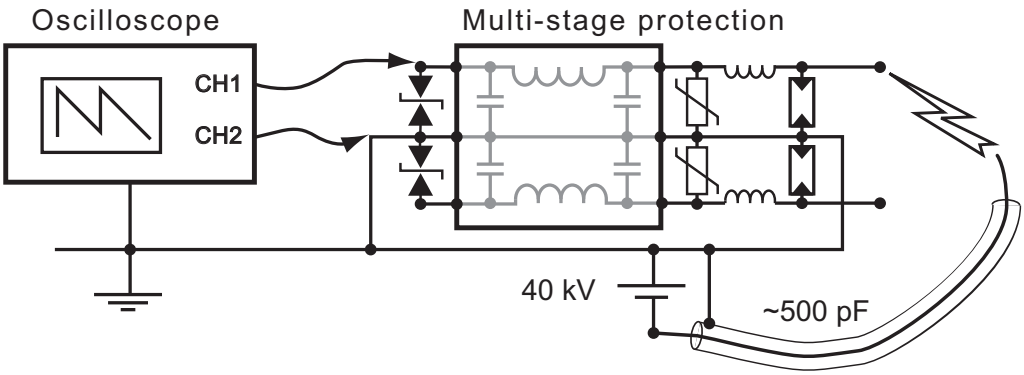

Figure 3.9: The differential measurement setup for the transient suppressor tests. Two voltage probes are used to measure the potential difference over the transient suppressor.

The transient currents in a breakdown are so fast and large that not even a solid grounding can prevent the ground potential from rising. Therefore the measurements over the suppressor have to be done in a differential configuration. The measurement setup (Fig. 3.9) consists of two passive high voltage probes and a digital storage oscilloscope with high sampling speed and a capability for online subtraction between the two input channels. The probes are capable for the measurements of transients with leading edge length down to 7 ns (TES TEC HVP-15HF) [44] and are usable up to peak voltages of 15 kV with a bandwidth of 50 MHz.

In the actual configuration of power supplies in the lifetime beam the potential rise of the grounding is not harmful as long as the casings of the power supplies are grounded sufficiently to the HV platform.

The multi-stage protectors with different values of the isolation inductances between the protection stages were tested. With the recommended inductance isolation [45], i.e. inductance of 10 μH between a GDT and a varistor and 5 μH between a varistor and an avalanche diode, and using an additional preinductance of 5 μH, residual voltages with an amplitude of 300 V were measured. The effect of isolation inductances was observed not to be significant. With isolation inductances of 1 μH, a residual voltage of 400 V was measured. The length of the residual transient was order of $\sim$0.2 μs. This kind of transient, with the energy content estimated to be in the mJ range, was considered harmless for the power supplies used in the lifetime beam.

To complete the transient suppressor tests the actual power supplies used in the lifetime beam were exposed to the residual transients. The voltage probe system and the oscilloscope in the measurement setup described in Fig. 3.9 were replaced by a power supply driving one of the Helmholtz coils used in the beamline. Both types of the low DC voltage power supplies utilized were tested: the linear power supplies used for low current correction coils and the switched-mode power supplies for high current Helmholtz coils. The tests proved that both power supply types, protected by the transient suppressors, were able to sustain repetitive surge currents with the energy of approximatively 0.5 Joules.

Chapter 4

Studies in indium nitride

The studies in indium nitride (InN) form the second part of this thesis. The Doppler broadening measurements have been done with the conventional slow positron beam. The effects of V/III molar ratio and growth temperature in MOCVD-grown InN and irradiation induced defects in MBE-InN are studied. This chapter refers to Publs. V and VI.

4.1 Introduction

The III-nitride semiconductors, especially gallium nitride (GaN) and aluminum nitride (AlN), have long been under intensive research due to their attractive properties for optoelectronics and high-power electronics applications [46]. InN had been outside the research focus for long. However, in 1993, the success of GaInN-based LEDs gave rise to the interest towards InN.

The growth of high quality InN is rather difficult due to the high equilibrium vapor pressure of nitrogen over InN [47]. The lack of high quality material has been an impediment for the proper determination even of the fundamental properties of the material. Bulk samples are still unavailable but high quality films can nowadays be grown on sapphire with molecular beam epitaxy (MBE) [48, 49] and by metal-organic chemical vapor deposition (MOCVD) [50, 51].

Much of the research on this material has been focused on the magnitude of the band gap. After improvements in the quality of InN layers band gap energy is strongly believed to be ∼0.7 eV [52–57] instead of the long-lived ∼1.9 eV [58–60]. Due to the discovery of the narrow band gap of InN, and the possibility of the III-N ternary alloy systems to extend the spectral range from infrared to deep ultraviolet, attraction towards InN was increased. With proper alloying with GaN

(E_g=3.4 eV [61]) and AlN (E_g=6.2 eV [62]) a very wide band gap continuum can be achieved. Especially advantageous this is for multijunction solar cell technology [63]. InN can also be used for light-emitting diodes (LEDs) and laser diodes (LDs). The photoluminescence (PL) peak of InN has been measured to be very stable as a function of temperature, which can open the way for optical communication applications [64].

InN has also superb electron transport characteristics, i.e. high mobility and high saturation and peak velocities at room temperature [65–67]. These properties originate from the low effective mass [57, 68] of electrons. Electron mobility as high as 2200 cm^2/Vs has already been experimentally observed [69]. Due to these properties InN is a promising material for high electron mobility transistors (HEMTs) and field-effect transistors (FETs) with anticipated cut-off frequencies as high as 2.5 THz [70]. These devices are used in high speed applications, e.g. in telecommunications industry and military technology.

The quality of InN has improved dramatically during the recent years, but there are still some impediments to the realization of actual InN devices. These originate from the low growth and dissociation temperatures and also large differences in the lattice constants between InN and other III-V semiconductors. Also unintentional n-type doping of as-grown material is still not fully controlled. The origin of the donor states is not known, but the calculations show that the formation energies for O_N and Si_{In} are the lowest of the donor-type defects [71]. On the other hand, first evidence of p-type doping of InN has been reported recently [72], which is very promising for the fabrication of electronic and optoelectronic devices using InN.

The properties of InN are greatly affected by the layer thickness [73, 74] and the substrate material, as well as the growth temperature [48] and the stoichiometry [75, 76]. The effect of different growth stoichiometry, i.e. V/III molar ratio, and growth temperature on point defect formation in MOCVD-grown InN is studied in Publ. V. An additional advantage of InN is its high radiation-hardness [63], which is valuable especially in possible space applications. In Publ. VI the point defects are studied in MBE-grown InN irradiated with 2 MeV $^4He^+$.

4.2 Effects of InN growth stoichiometry

4.2.1 Samples

The measured samples (Table 4.1) were grown by metal-organic chemical vapor deposition (MOCVD) at Université Montpellier II [50]. The thicknesses of the InN layers grown directly on sapphire substrate varied from 200 nm to 1400 nm

Table 4.1: Growth parameters of the measured samples and the vacancy concentrations estimated from the results of positron annihilation measurements.

Sample No.	V/III molar ratio	Thickness (μm)	Growth temperature (°C)	Vacancy concentration (cm^{-3})
1	24 000	0.2	550	9×10^{16}
2	15 000	<0.3	550	7×10^{16}
3	10 000	0.3	550	2×10^{17}
4	4 840	0.6	550	9×10^{16}
5	4 840	0.5	625	4×10^{17}
6	4 840	0.6	600	7×10^{17}
7	3 650	1.4	550	8×10^{16}
8	3 267	0.9	550	1×10^{17}

and the V/III molar ratios used during the growth process were between 3300 and 24000. Growth temperatures were in the range of 550°C–625°C. An MBE-grown sample with no positron-trapping vacancy defects, according to previous positron lifetime and Doppler broadening studies [73, 77], was used as a reference sample. The samples grown at the most In-rich conditions, had visible droplets at the surface, identified as metallic indium.

4.2.2 Results and discussion

Figure 4.1 presents the measured S parameters (in samples with V/III $>$ 4000) as a function of positron implantation energy (i.e. depth scan). The S parameter at the sample surface (E<2 keV) is high, reflecting the low electron density at the surface. The plateau starting at energies of 2 keV corresponds to the InN layer. At higher energies the S parameter decreases as the positrons start to reach the substrate.

The presence of vacancy defects can be seen as higher values of the layer specific S parameters. To investigate the type of vacancy, the layer specific S and W parameters were plotted in an (S,W) plot (Fig. 4.2) [5]. When positron trapping vacancies are not present in the studied sample, values S_b and W_b for low and high electron-momentum parameters are obtained. Similarly, in a sample where all the positrons get trapped at vacancies (positron saturation trapping) we get S_d and W_d characterizing the vacancy. All the samples containing the same type of vacancies at variable concentrations fall on a same line in the (S,W) plot. The slope of the line can be used as a fingerprint for the vacancy type [4].

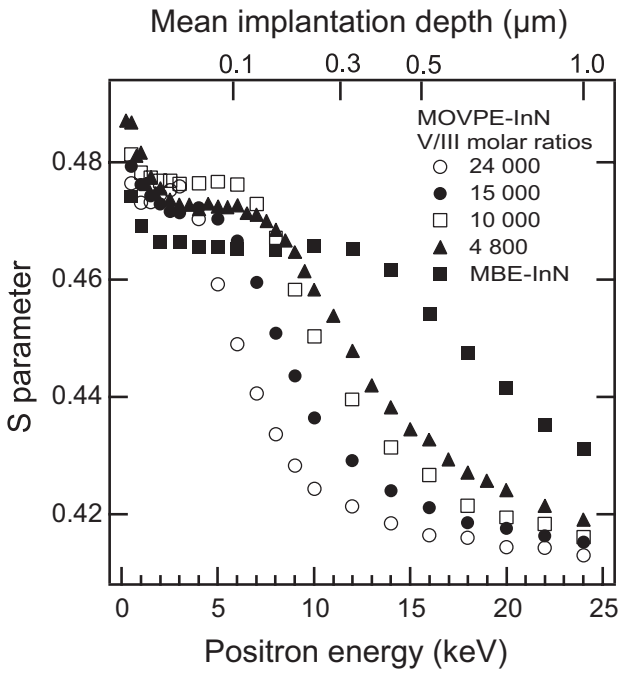

Figure 4.1: The S parameter as a function of positron implantation energy in samples grown with different V/III molar ratio.

It is known from previous studies of InN that indium monovacancies produce vacancy specific parameters $S_V = 1.049 \times S_b$ and $W_V = 0.79 \times W_b$ [73]. From Fig. 4.2 we obtain that all layer specific points from all the samples fall on the same line whose slope equals with the previous studies observed for indium monovacancy. The two samples with smallest V/III ratio showed slightly different behavior. A rise in the S parameter close to the substrate interface was observed. These higher values were also plotted in the (S,W) plot producing a straight line with the parameters of the defect-free MBE-InN. The smaller slope indicates that vacancy clusters are formed near the interface.

The vacancy concentrations are estimated from the Doppler parameters using the standard positron trapping model [4] with positron trapping coefficient of 2×10^{15} cm^{-3} for In monovacancies. The In vacancy concentrations vary from 7×10^{16} cm^{-3} to 2×10^{17} cm^{-3} in all samples grown at 550°C. Interestingly, these densities are very similar to those detected in MBE samples of the same thicknesses (200–300 nm) [73, 77]. This suggests that indium vacancy formation is dominated by thickness-dependent properties, such as strain or dislocation density, and that it is less dependent on growth thermodynamics or stoichiometry. In fact, the calculated formation energies of In vacancies are high [71], which is in

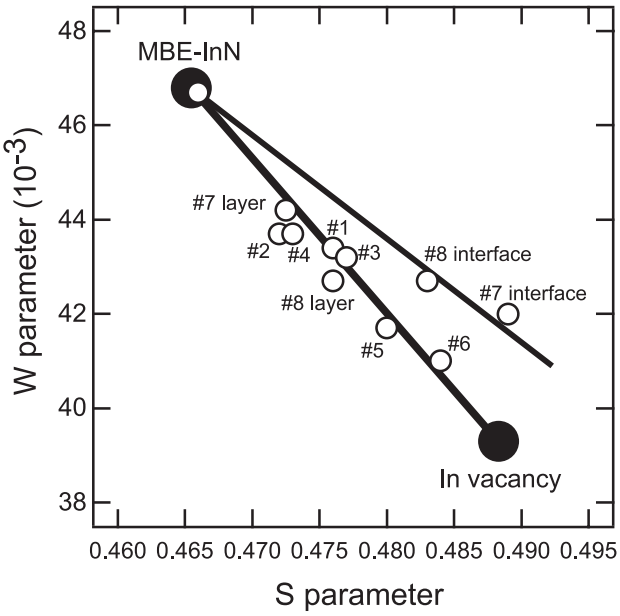

Figure 4.2: The W parameter as a function of the S parameter. The linearity between the layer specific parameters indicate that the same kind of vacancy (indium vacancy) is present in all the layers. The S parameters for vacancy clusters, formed close to the interface, form a line with a gentler slope and are thus distinguishable from the indium vacancies.

agreement with the positron result showing their absence in thick ($\gtrsim$1 μm) MBE layers [73, 77].

Additionally, the S parameters were measured as a function of positron implantation energy in samples grown at different temperatures. The vacancy concentrations in these samples were estimated and observed to increase from 10^{17} cm^{-3} to 10^{18} cm^{-3} when the growth temperature was increased from 550°C close to the decomposition temperature of 625°C. More indium lattice sites are thus left empty when the growth takes place close to the decomposition temperature of InN, perhaps because of the limited sticking of indium on the growth surface.

4.3 Radiation damage produced by 2-MeV He^+-ions

4.3.1 Samples

Seven MBE-grown InN samples were irradiated at Lawrence Berkeley National Laboratory at different fluences (5×10^{13} cm^{-2}–2×10^{16} cm^{-2}). The samples were

0.6 μm thick, except two (ϕ=5×10^{13} cm^{-2} and 9×10^{15} cm^{-2}), which were 2.7 μm thick. The residual electron concentration in as-grown InN was 1×10^{18} cm^{-3} and the room-temperature electron mobility 1560 cm^2/Vs, based on Hall measurements. The electron concentration increased in the irradiation up to ∼4×10^{20} cm^{-3} while the mobility decreased to ∼60 cm^2/Vs. For comparison, we studied also similarly irradiated (2.7 μm thick) GaN samples grown by metal-organic chemical vapor deposition (MOCVD), which turn from slightly n-type to semi-insulating in the irradiation.

4.3.2 Results and discussion

The S and W (not shown) parameters in the as-grown GaN sample coincide with those measured in a high-quality GaN samples grown by hydride vapor phase epitaxy, where positrons are known to annihilate only in the free state [78]. The InN sample irradiated to the fluence of 5×10^{13} cm^{-2} exhibited a slightly lower S parameter than the previously used InN reference [73, 79]. We interpret this to originate from the greater thickness of the current sample (2.7 μm), since in the quality of the MBE grown InN is known to improve with increasing layer thickness [73]. In addition, as shown below, the vacancy concentration produced in InN with this fluence should be below the detection limit of the positron method at room temperature. This sample is thus taken as a reference for the InN lattice in this work.

The In vacancy specific parameters determined in previous studies in InN, namely S_v=1.049×S_b and W_v=0.79×W_b [73] are used. These parameters are shown together with the measured parameters from the irradiated InN samples in Fig. 4.3. As all the points fall on the same straight line connecting the InN bulk and In vacancy specific parameters, the observed vacancy defects are identified as the In vacancy. Interestingly, the In vacancy concentration seems to saturate at the fluence of 2×10^{15} cm^{-2}.

In order to determine the possible effect of negative ions on the room temperature data, four irradiated InN samples at temperatures ranging from 20 K to 300 K (Fig. 4.4) were measured. The S parameter measured in the layer decreases with decreasing temperature, indicating that negative ions compete with vacancies in trapping of positrons at low temperatures, as the negative ions produce the annihilation parameters of the defect-free lattice. At temperatures near 300 K, the S parameter changes only slightly, indicating that mostly vacancy defects trap positrons. The plateau at low temperatures further indicates that temperature dependences of the trapping rates of vacancies and negative ions are the same ($T^{-1/2}$, see Ref. [6]) and thus the vacancy defects are negatively charged.

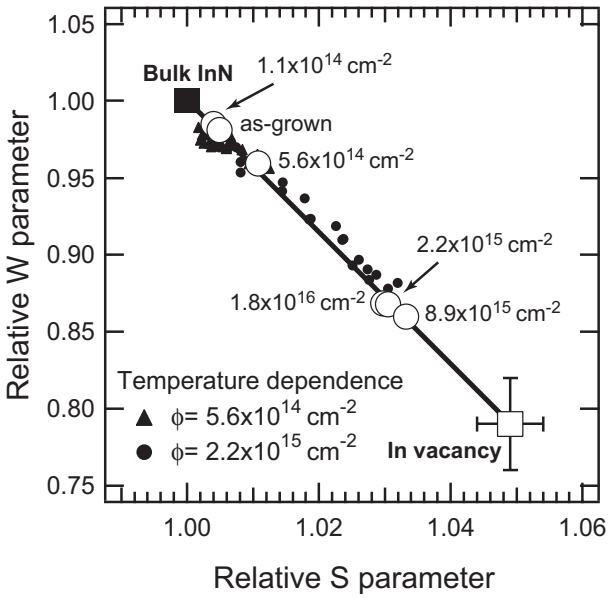

Figure 4.3: The relative W parameter as a function of the relative S parameter in He^+ irradiated layers. The parameters obtained in two samples measured at different temperatures are also shown.

The vacancy concentrations in the samples can be estimated from the layer specific S parameters using the standard positron trapping model with a positron trapping coefficient of 2×10^{15} cm^{3}s^{-1} [4]. Figure 4.5 shows the estimated vacancy concentrations as a function of irradiation fluence for InN and GaN samples. [V_{In}] saturates to $4{\times}10^{17}$ cm^{-3} at the fluence of $2{\times}10^{15}$ cm^{-2}. This result clearly indicates that the saturation of the free electron concentration [80] can not be due to the In vacancy production. The Ga vacancy concentration in GaN increases linearly as a function of irradiation fluence. All the positrons annihilate as trapped at Ga vacancies in the three most heavily irradiated samples, and hence only a lower limit of $\sim 1 \times 10^{19}$ cm^{-3} can be given for those samples.

The introduction rates (defined as $\Sigma_V = [V]/\phi$) of In and Ga vacancies can be estimated from the data in Fig. 4.5. The introduction rate of the In vacancies is $\Sigma_{V,\mathrm{In}} = 100$ cm^{-1}, and that of the Ga vacancies is $\Sigma_{V,\mathrm{Ga}} = 3600$ cm^{-1}. On the other hand, the introduction rate of the In vacancies, which is almost two orders of magnitude lower than that of the Ga vacancies, suggests that the observed In vacancies are not primary defects produced in the irradiation. In addition, their final concentration and low introduction rate clearly indicate that the saturation of the free electron concentration at 4×10^{20} cm^{-3} [80] (the donor introduction rate is 3.5×10^4 cm^{-1} [72]) is not due to In vacancy production.

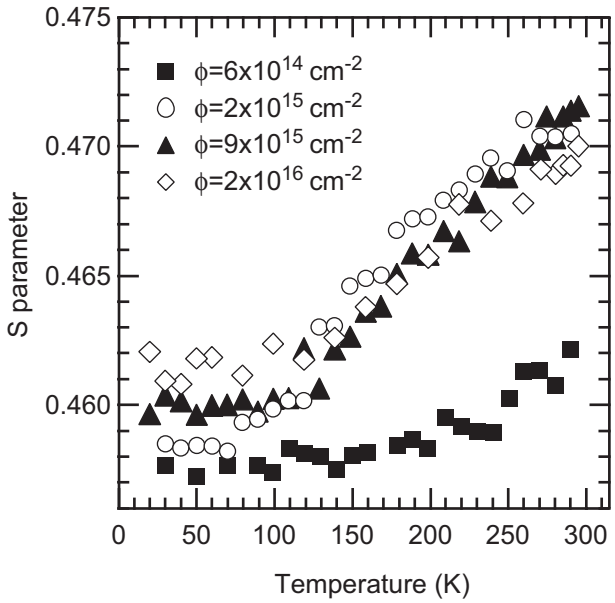

Figure 4.4: The S parameters measured in the InN samples (fluences from 6×10^{14} cm^{-2} to 2×10^{16} cm^{-2}) as a function of temperature. The behavior is typical for negative ion type defects competing with vacancies in positron trapping.

To find out if the negative ions could be the compensating defects giving rise to the saturation of free electron concentration in InN, we estimate the negative ion concentrations in the samples irradiated to the fluences of 6×10^{14} cm^{-2} – 2×10^{16} cm^{-2}. The concentrations can be estimated using the temperature-dependent trapping model [4]: the negative ion concentrations in all the four measured samples are in the range of $0.8 - 3\times10^{18}$ cm^{-3} (Fig. 4.5), using the same positron trapping coefficient for negative ions as for negatively charged vacancies. Because the concentration is not increasing significantly with the irradiation fluence, this suggests that negative ions could not explain the compensating effect obtained in the irradiated InN.

From the sample with the two lowest He^+ fluences where the negative ion concentration was measured, we can estimate that the introduction rate is about $\Sigma_{\mathrm{ion}} = 2000$ cm^{-1}, which is still an order of magnitude too low to explain the saturation of the electron concentration. However, the decrease in the apparent negative ion concentration in the samples with the highest fluences points towards an explanation of this discrepancy. As the donor concentration is high (above 10^{19} cm^{-3}) already after the irradiation fluence of 5×10^{14} cm^{-2}, it is likely that the negative charge of the negative ions is screened by the very high

free electron concentration. This screening becomes naturally even more efficient at higher fluences, finally causing the apparent negative ion concentration to even decrease with increasing fluence. Hence the negative ion concentrations may be severely underestimated. On the other hand, this screening of the negative charge would not have any significant effect on the positron trapping at vacancies, as the difference in the trapping coefficients between negative and neutral vacancies is only about a factor of 2 at room temperature.

Based on the Hall mobility, the actual concentration of negatively charged defects is indeed likely to be higher than the apparent concentration of negative ions at high fluences. In a previous study [73], the Hall mobility of 200 cm^2/Vs was correlated with a negative defect (In vacancy) concentration of about 10^{19} cm^{-3}. In the present work the mobility is 60 cm^2/Vs at its lowest, suggesting a concentration of (negative) scattering centers of an order of magnitude higher. As the In sublattice is clearly quite resistant to the radiation damage based on the low In vacancy concentration, it seems that either the In interstitial or the In vacancy (or both) are rather mobile at room temperature, resulting in fast recombination of the Frenkel pairs or defect out-diffusion to the sample surface. Hence it seems likely that both the donors and dominant compensating defects (acceptors) originate from the damage created in the N sublattice. As the V_N are likely to be the donor defects, it seems that the dominant compensating defect introduced in the irradiation could be related to the N interstitial.

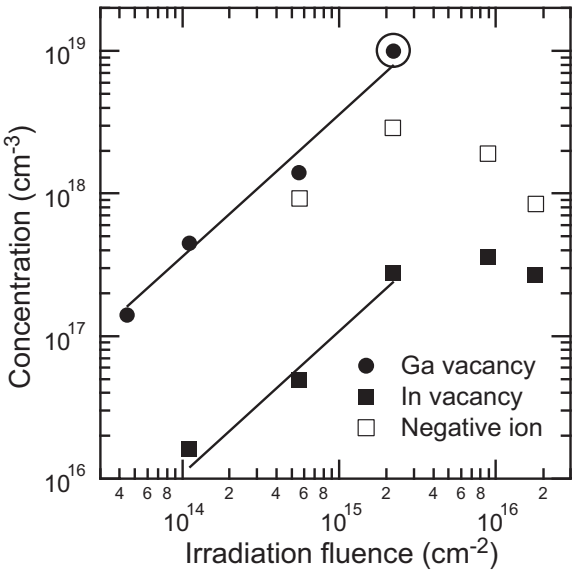

Figure 4.5: Estimated indium and gallium vacancy concentrations as well as negative ion concentration in InN and GaN at different irradiation fluences. The vacancy production rates are 100 cm^{-1}, 3600 cm^{-1} and 2000 cm^{-1}, respectively.

Chapter 5

Summary

In this work the design of the TKK pulsed positron lifetime beam is briefly reviewed and the unique high voltage configuration and challenges of HV design of the system are discussed in detail.

The timing properties of the lifetime beam were determined using electrons and positrons with a fast multichannel plate and BaF_2 scintillator as detectors. With a MCP the time resolution of the lifetime beam was measured to be 160 ps for electrons and 170 ps for positrons. The peak-to-background ratios were respectively $\sim$5000 and $>$1000. Positron lifetime measurement was demonstrated by measuring a lifetime spectrum in MCP.

Thorough high voltage withstand tests were carried out for every component in the HV system of the lifetime beam. They were found to be HV proof. Additionally, to protect electronics against breakdown induced transients, multi-stage transient suppressors were constructed and tested. The residual transient energy in the range of mJ was observed low enough for the power supply protection.

Positron annihilation measurements were performed in MOCVD-InN. Vacancy defects were observed at concentrations of $\sim 10^{17}$ cm^{-3} and identified as indium vacancies. The indium vacancy concentration is almost independent on the V/III molar ratio at 4800–24000. At lower ratios, below 4000, the In droplet formation is accompanied by the formation of vacancy clusters. The In vacancy formation depends on the growth temperature. The concentration was observed to increase from 10^{17} cm^{-3} to 10^{18} cm^{-3} when the growth temperature was increased from 550°C close to the decomposition temperature of 625°C.

Finally we studied 2 MeV $^4He^+$ irradiated InN grown by molecular beam epitaxy and GaN grown by metal-organic chemical vapor deposition. In GaN, the Ga vacancies act as important compensating centers in the irradiated material,

introduced at a rate of 3600 cm^{-1}. The In vacancies are introduced at significantly lower rate of 100 cm^{-1} making them negligible in the compensation of the irradiation-induced additional n-type conductivity. On the other hand, negative non-open volume are introduced at a rate higher than 2000 cm^{-1}. We propose that these defects are related to N interstitials and ultimately limit the free electron concentration at high irradiation fluences.

Bibliography

[1] D. Schödlbauer, P. Sperr, G. Kögel, and W. Triftshauser, Nuclear Instruments & Methods B **34**, 258 (1988).

[2] R. Suzuki *et al.*, Japanese Journal of Applied Physics **30(3B)**, L532 (1991).

[3] F. Tuomisto *et al.*, Physica Status Solidi B **240**, 289 (2003).

[4] K. Saarinen, P. Hautojärvi, and C. Corbel, in *Identification of Defects in Semiconductors* (Edited by M. Stavola, Academic Press, N.Y., 1998. ISBN 0-12-752165-8), p. 209.

[5] L. Liszkay *et al.*, Applied Physics Letters **64**, 11 (1994).

[6] M. J. Puska, C. Corbel, and R. M. Nieminen, Physical Review B **41**, 9980 (1990).

[7] K. G. Lynn, B. Nielsen, and J. H. Quateman, Applied Physics Letters **47**, 239 (1985).

[8] E. Gramsch, J. Throwe, and K. G. Lynn, Applied Physics Letters **51**, 1862 (1987).

[9] H. M. Weng *et al.*, Nuclear Instruments & Methods B **225**, 397 (2004).

[10] F. Reurings *et al.*, Applied Surface Science **252**, 3154 (2006).

[11] S. J. Gilbert, C. Kurz, R. G. Greaves, and C. M. Surko, Applied Physics Letters **70**, 1944 (1997).

[12] K. G. Lynn, W. E. Frieze, and P. J. Schultz, Physical Review Letters **52**, 1137 (1984).

[13] A. P. Mills Jr., Applied Physics A **22**, 273 (1980).

[14] K. Fallström and T. Laine, Applied Surface Science **149**, 44 (1999).

[15] A. Laakso, *Construction of a Pulsing System for Low-Energy Positrons*, Doctoral Thesis, Helsinki University of Technology, Laboratory of Physics, (2005).

[16] A. Pelli, *Pulssitetun positronisuihkun rakentaminen ja testaus*, Special assignment, Helsinki University of Technology, Department of Engineering Physics and Mathematics, (2001).

[17] Mini-Circuits, `www.minicircuits.com`, [cited 15.10.2006].

[18] J. Oila, *Kiihdytinrakenteen suunnittelu pulssitettua positronisuihkua varten*, Special assignment, Helsinki University of Technology, Department of Engineering Physics and Mathematics, (1997).

[19] Kimball Physics Inc., *Data sheet: Barium Oxide (BaO) Cathodes, ES-015*, `www.kimballphysics.com`, [cited 5.10.2006].

[20] Hamamatsu Photonics K.K., *Data sheet: F4655-12 (Rev. Jan 1996)*, `www.datasheetcatalog.com`, [cited 5.10.2006].

[21] F. Reurings and A. Laakso, (submitted to Physica Status Solidi C).

[22] A. Pelli, Master's thesis, Helsinki University of Technology, Department of Engineering Physics and Mathematics, (2002).

[23] F. Paschen, Wied. Ann. **37**, 69 (1889).

[24] A. Schwaiger, *Elektrische Festigkeitslehre* (Springer-Verlag, Berlin, 1925).

[25] IEC Standard 60270 (third edition), *Partial Discharge Measurements*, International Electrotechnical Commission (IEC), Geneva, Switzerland, 2000.

[26] M. Aro *et al.*, *Suurjännitetekniikka* (Otatieto, Jyväskylä, 2003. ISBN 951-672-320-9).

[27] R. V. Latham, *High Voltage Vacuum Insulation: The Physical Basis* (Academic Press Inc., London, 1981. ISBN 0-12-437180-0).

[28] M. D. Noskov, M. Sack, A. S. Malinovski, and A. J. Schwab, Journal of Physics D: Applied Physics **34**, 1389 (2001).

[29] R. Vogelsang, B. Fruth, T. Karr, and K. Fröhlich, European Transactions on Electrical Power **15**, 271 (2005).

[30] Vishay Intertechnology, Inc., *Data-sheet: VR68, High Ohmic, High Voltage Resistors (Revision 08-Apr-05)*, `www.vishay.com`, [cited 29.9.2006].

[31] Hipotronics Inc., `www.hipotronics.com`, [cited 27.9.2006].

[32] Tera Analysis Ltd., QuickField 5.1, 2D FEM analysis program.

[33] Goodfellow Cambridge Limited, *Material properties: polyoxymethylene, copolymer*, `www.goodfellow.com`, [cited 27.9.2006].

[34] Ohmite Mfg. Co., *Data-sheet: Mini-Mox Resistors*, `www.ohmite.com`, [cited 29.9.2006].

[35] American Technical Ceramics Corp., *Data-sheet: ATC 100 E series capacitors (Rev. G 12/04)*, `www.atceramics.com`, [cited 27.9.2006].

[36] IEC Standard 60071-1, Insulation co-ordination - Part 1: Definitions, principles and rules, 1993.

[37] J. Annanpelto *et al.*, *Rakennusten ylijännite- ja ukkossuojaus* (Sähkö- ja teleurakoitsijaliito STUL ry, Espoo, 2005. ISBN 952-5382-70-2).

[38] *Transient Voltage Suppression, 3rd Edition*, General Electric Company, U.S.A, Semiconductor Products Department, New York, 1982.

[39] Epcos AG, *Data-sheet: 2-Electrode-Arrester, N81-A90X (Issue 03, 26.04.2002)*, `www.epcos.com`, [cited 3.10.2006].

[40] Epcos AG, *Data-sheet: Leaded Varistors, Standard D Series, S05K25 (Issue 03, 26.04.2002)*, `www.epcos.com`, [cited 3.10.2006].

[41] STMicroelectronics, *Data-sheet:TRANSIL 1.5KE33A*, `www.st.com`, [cited 15.10.2006].

[42] Fischer Custom Communications, Inc., *Spikeguard specifications*, `www.fischercc.com`, [cited 17.10.2006].

[43] F. H. Kreuger, *Industrial High Voltage Part II* (Delft University Press, Delft, 1992. ISBN 90-6275-562-3).

[44] TESTEC Elektronik GmbH, *Product information: TT-HVP 15HF*, `www.testec.de`, [cited 2.10.2006].

[45] J. Elovaara *et al.*, *Ylijännitesuojaus* (Suomen Sähköurakoitsijaliitto ry, Espoo, 1994. ISBN 952-9756-06-2).

[46] S. Strite and H. Morkoç, Journal of Vacuum Science and Technology B **10**, 1237 (1992).

[47] O. Ambacher *et al.*, Journal of Vacuum Science and Technology B **14**, 3532 (1996).

[48] H. Lu *et al.*, Applied Physics Letters **77**, 2548 (2000).

[49] Y. Saito *et al.*, Japanese Journal of Applied Physics **40(2)**, L91 (2001).

[50] B. Maleyre, O. Briot, and S. Ruffenach, Journal of Crystal Growth **269**, 15 (2004).

[51] O. Briot, B. Maleyre, and S. Ruffenach, Applied Physics Letters **83**, 2919 (2003).

[52] T. Inushima *et al.*, Journal of Crystal Growth **227**, 481 (2001).

[53] V. Y. Davydov *et al.*, Physica Status Solidi B **229**, R1 (2002).

[54] T. Matsuoka *et al.*, Applied Physics Letters **81**, 1246 (2002).

[55] J. Wu *et al.*, Applied Physics Letters **80**, 3967 (2002).

[56] Y. Saito *et al.*, Physica Status Solidi B **234**, 796 (2002).

[57] W. Walukiewicz *et al.*, Journal of Crystal Growth **269**, 119 (2004).

[58] T. L. Tansley and C. P. Foley, Journal of Applied Physics **59**, 3241 (1986).

[59] K. Osamura, K. Nakajima, and Y. Murakai, Solid State Communications **11**, 617 (1972).

[60] K. S. A. Butcher *et al.*, Materials Science in Semiconductor Processing **6**, 351 (2003).

[61] H. P. Maruska and J. J. Tietjen, Applied Physics Letters **15**, 327 (1969).

[62] W. M. Yim *et al.*, Journal of Applied Physics **44**, 292 (1973).

[63] J. Wu *et al.*, Journal of Applied Physics **94**, 6477 (2003).

[64] T. Matsuoka *et al.*, Journal of Crystal Growth **269**, 139 (2004).

[65] B. E. Foutz, S. K. O'Leary, M. S. Shur, and L. F. Eastman, Journal of Applied Physics **85**, 7727 (1999).

[66] S. K. O'Leary, B. E. Foutz, M. S. Shur, and L. F. Eastman, Applied Physics Letters **87**, 222103 (2005).

[67] K. T. Tsen *et al.*, Applied Physics Letters **86**, 222103 (2005).

[68] B. Rezaei, A. Asgari, and M. Kalafi, Physica B **371**, 107 (2006).

[69] W. Walukiewicz *et al.*, Journal of Crystal Growth **288**, 278 (2006).

[70] S. K. O'Leary, B. E. Foutz, M. S. Shur, and L. F. Eastman, Applied Physics Letters **88**, 152113 (2006).

[71] C. Stampfl *et al.*, Physical Review B **61**, 7846 (2000).

[72] R. E. Jones *et al.*, Physical Review Letters **96**, 125505 (2006).

[73] J. Oila, A. Kemppinen, A. Laakso, and K. Saarinen, Applied Physics Letters **84**, 1486 (2004).

[74] R. S. Fareed *et al.*, Applied Physics Letters **84**, 1892 (2004).

[75] A. Koukitu, N. Takahashi, and H. Seki, Japanese Journal of Applied Physics **36(2)**, L1136 (1997).

[76] T. Matsuoka, in *GaN Related Materials* (Edited by S. J. Pearton, Gordon and Breach, New York, 1997. ISBN 90-5699-516-2), p. 53-59.

[77] A. Laakso *et al.*, Journal of Crystal Growth **41**, 41 (2004).

[78] F. Tuomisto *et al.*, Applied Physics Letters **86**, 031915 (2005).

[79] A. Pelli *et al.*, Applied Physics Letters **89**, 011911 (2006).

[80] S. X. Li *et al.*, Physical Review B **71**, R161201 (2005).